ORNL/TM-2021/2110

A Vorticity Description of the Nuclear Cloud

Pablo Moresco

June 2022

OAK RIDGE National Laboratory

ORNL IS MANAGED BY UT-BATTELLE LLC FOR THE US DEPARTMENT OF ENERGY

ORNL/TM-2021/2110

Nuclear Nonproliferation Division

A VORTICITY DESCRIPTION OF THE NUCLEAR CLOUD

Pablo Moresco

June 2022

Prepared by
OAK RIDGE NATIONAL LABORATORY
Oak Ridge, TN 37831-6283
managed by
UT-Battelle LLC
for the
US DEPARTMENT OF ENERGY
under contract DE-AC05-00OR22725

CONTENTS

LIST OF FIGURES

LIST OF TABLES

ACKNOWLEDGMENTS

This work was funded by the Office of Nuclear Detonation Detection - Forensics Program within the US Department of Energy's National Nuclear Security Administration as part of the Water-Surface-Burst Fallout Model project.

ABSTRACT

We describe a model of the nuclear cloud in terms of the vorticity field associated with a buoyant vortex ring. A series of physical approximations are introduced that lower computational costs and render the model amenable for operational use. The determination of model parameters from the yield and emplacement of the weapon is also discussed.

1. INTRODUCTION

During the initial minutes after a nuclear detonation above ground level, the most prominent feature is the development of a convective cloud, made visible mainly by dust and weapon debris particles and in some cases water condensation. The ability to predict the characteristics of the nuclear cloud from the weapon yield and emplacement, as well as the prevailing atmospheric conditions at the time of the burst, is an important component in descriptions of the distribution of fallout (Foster (1982)) and has a direct impact on the planning of activities associated with emergency response and the collection of samples for forensic analysis.

A nuclear detonation above the ground can be approximated by an almost instantaneous release of energy in a confined volume of air, resulting in a high temperature and low density perturbation of the atmosphere. This fireball, which is vertically accelerated by buoyancy forces, also entrains air at such a fast rate that after a short transient its speed of ascent decreases monotonically with time, and the resulting cloud eventually reaches a stabilization height.

Attempts at describing the nuclear cloud were initiated shortly after the development of nuclear weapons. In a technical report, Taylor (1945) proposed a model based on the observations and theory by Schmidt (1941) on the steady convective flows produced by heated wires in a uniform atmosphere. These types of flows, where there is a continuous release of buoyancy, are commonly called *plumes*. Schmidt's description assumes the flow to be similar along the distance from the source (i.e., the distributions of velocity and density to have the same shape at all heights, apart from a scale factor). His theory follows the idea of turbulent mixing as driven by eddies with a characteristic size, the mixing length (Pope (2000)), which he took to be proportional to the lateral dimension of the plume. Schmidt also used the vertical velocity of the flow averaged across the plume to define a characteristic velocity, and from its gradient in the horizontal direction a turbulent viscosity, responsible for the lateral transport of heat and momentum.

Taylor (1945) proposed a simplified description of the plume flow, which lacks the detailed mechanism proposed by Schmidt, but is easier to extend to nonuniform atmospheres. His description is based on the assumption that, at a given height, the inflow velocity of the entrained fluid is proportional to a characteristic velocity at that height. He showed that with this entrainment hypothesis the model results for the plume flow have the same functional dependencies as Schmidt's theory, while being simpler to extend to stratified environments, as it was later done by Morton et al. (1956).

In Taylor's model for plumes, the steady flow condition leads to the conclusion that, in uniform atmospheres, the width of the plume (r) at a given height (z)* satisfies

$$r = \alpha z, \tag{1}$$

where α is the entrainment parameter. This relation implies that the border of the plume forms a straight line, with α being the tangent of the angle subtended with the axis of symmetry.

*Vertical distance measured from a virtual, zero-size source.

Very shortly after a nuclear explosion and the initial deposition of energy, a rarefaction wave propagates to the interior of the heated volume resulting in the formation of a low density region, which bears similarities to the initial condition usually assumed for thermals in atmospheric flows (Taylor (1950a,b); Scorer (1957)).[†] One important difference between plumes and thermals is that the latter lack the temporal time scale prescribed by the rate of buoyancy release. To apply the similarity model described above to thermals, it is necessary to introduce an additional assumption, and Taylor (1945) proposed to take the volume of the density perturbation to be spherical and the characteristic dimension to be its radius. Although the shape of the nuclear cloud is usually not spherical, the main requirement in this formulation is that a representative length scale be chosen so that the ratio of the surface to the volume of the buoyant mass can be described as the ratio of the square to the cube of that length (Morton et al. (1956); Turner (1986)). Under these assumptions, relation (1) can again be derived from the equations of motion and in this case is also valid in stratified environments.[‡] Experimentally, thermals have been found to entrain ambient fluid faster than plumes (larger α) but at a rate that is more sensitive to initial conditions (Turner (1973)). As explained below, thermals can be described as buoyant vortex rings whose dynamics govern the entrainment process.

Under the Boussinesq approximation (see Section 2), equation (1) can be put in the form of a volume conservation relation (2), and together with expressions for the conservation of momentum (3) and buoyancy (4), a system of ordinary differential equations is obtained that describes the evolution of the cloud, namely its radius $\underline{r}$ and center height $\underline{z}$, with time t, from a given initial condition (Taylor (1945)):

$$\frac{d}{dt}\left(\frac{4}{3}\pi\underline{r}^3\right) = 4\pi\alpha u\underline{r}^2, \tag{2}$$

$$\frac{d}{dt}\left(\underline{r}^3 u\right) = \frac{g}{T}(\theta-\theta_0)\underline{r}^3, \tag{3}$$

$$\frac{d}{dt}\left(\underline{r}^3\theta\right) = 3\alpha\underline{r}^2 u\theta_0, \tag{4}$$

$$\frac{d\underline{z}}{dt} = u, \tag{5}$$

where u and θ are the vertical velocity and (excess) potential temperature of the cloud, θ_0 is the ambient potential temperature at the height of the cloud, T is a reference potential temperature, and g is the acceleration of gravity.

Refinements to this model that include additional effects such as drag forces and turbulence parameterizations have been developed and form the basis of descriptions, with low computational cost, used in some operational codes that describe the nuclear cloud (Norment (1979)). Other formulations of the cloud evolution also based on Schmidt's ideas were put forward by Sutton (1950), who proposed to treat the entrainment phenomenon as a diffusion process (Sutton (1947)), and by Machta (1950), who expressed the entrainment rate as a constant fraction of the volume of the cloud.

There is abundant empirical evidence that instantaneous releases of buoyant fluid tend to develop recirculating flows akin to those present in vortex rings,[§] and Turner (1957) suggested using the

[†]Thermals are generally considered to be fundamental components in the development of cumuli cloud in the atmosphere (Pergaud et al. (2009)).

[‡]In this approach, the initial volume of the fireball or thermal is considered to be negligible in comparison to that of the cloud at a later time, implying that the initial condition does not introduce a length scale and the radius and height of the cloud have to be proportional.

[§]The pictorial evidence from the nuclear tests (Kuran (2006)) also supports this hypothesis.

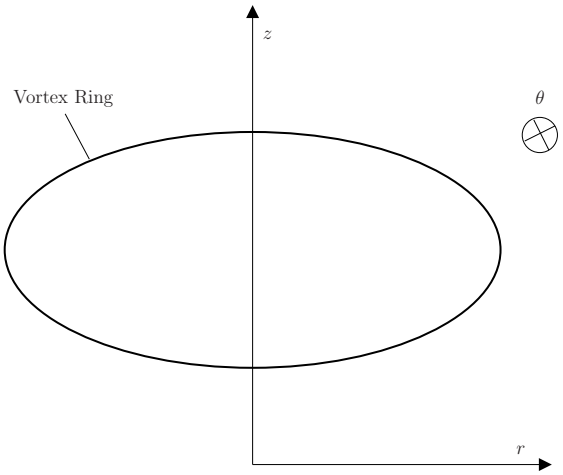

Figure 1. Description of a cylindrical coordinate system aligned with the axis of symmetry of the vortex ring, with z, r and θ the axial, radial and azimuthal coordinates, respectively.

characteristics of this type of flows to describe thermals and buoyant clouds. For an axisymmetric vortex ring in an infinite fluid of constant density ρ, the impulse can be written (Lamb (1932)[¶])

$$P = \pi\rho \iint_S r^2 \omega \, dzdr, \tag{6}$$

where r and z are the radial and axial cylindrical coordinates in a frame of reference aligned with the axis of symmetry of the ring (Figure 1), ω is the vorticity field, with component only in the azimuthal direction, θ, and S is an area of a meridional plane containing a cross section of the ring. If we define the ring radius, R, in terms of the centroid of vorticity according to

$$R^2 = \frac{1}{\Gamma} \iint_S r^2 \omega \, dzdr, \tag{7}$$

where Γ is the circulation of the ring,

$$\Gamma = \iint_S \omega dr dz \tag{8}$$

the impulse can be written

$$P = \pi\rho R^2 \Gamma. \tag{9}$$

This expression shows that, when written in terms of R, P is independent of the distribution of vorticity, and it only depends on the circulation of the ring. In a similar manner we can define the ring vertical position in terms of the vorticity centroid by

$$Z = \frac{1}{\Gamma R^2} \iint_S r^2 \omega \, z \, dr dz. \tag{10}$$

[¶]The impulse of the flow is defined by Lamb as the total mechanical impulse of the non-conservative body forces required to generate the motion instantaneously from rest.

If the density of the ring differs by a small amount, $\Delta\rho$, from the rest of the fluid so that the Boussinesq approximation is applicable, the buoyancy force acting on the ring changes its impulse according to

$$\frac{dP}{dt} = gV\Delta\rho, \tag{11}$$

where V is the volume of the ring.

In the case of uniform atmospheres, the experimental evidence indicates that buoyant vortex rings propagate with approximately constant circulation (Walters and Davidson (1963); Turner (1973); Zhao et al. (2013)). This is understood to be caused by the rapid growth of the radius of the ring, which counterbalances the diffusion of vorticity towards its axis, where vorticity cancellation could occur (Turner (1957); Maxworthy (1972)). Assuming Γ to be constant and using (9), we then have

$$\pi\rho\Gamma\frac{dR^2}{dt} = gV\Delta\rho, \tag{12}$$

which gives

$$\frac{dR}{dt} = \frac{B}{2\pi\Gamma}\frac{1}{R}, \tag{13}$$

with B the buoyant content of the ring defined by

$$B = \frac{gV\Delta\rho}{\rho}. \tag{14}$$

Relation (13) shows that the entrainment process is directly linked to the buoyant content of the ring. Whereas the turbulent character of the flow will be partly responsible for the mixing with ambient fluid, it has been shown that, in contrast to plumes, most of the contribution to the entrainment rate in thermals is due to the pressure changes associated to the radial growth governed by the buoyant character of the vortex ring (Lecoanet and Jeevanjee (2019)).

In general terms, vortex rings propagate along their axis with a self-induced velocity that can be written in the form

$$\frac{dZ}{dt} = \frac{\Gamma}{R}\mathcal{F}(\omega), \tag{15}$$

with $\mathcal{F}(\omega)$ a function of the vorticity distribution (Saffman (1992)). Combining (13) and (15) yields

$$\alpha = \frac{dR}{dt}\left(\frac{dZ}{dt}\right)^{-1} = \frac{B}{2\pi\Gamma^2}\frac{1}{\mathcal{F}(\omega)}, \tag{16}$$

which provides a link between the entrainment parameter used in the description of thermals and the properties of buoyant vortex rings. In the the case of stratified environments, density gradients will typically exist between the mass of fluid moving with the ring and its environment, and in stable atmospheres this density difference will result in the generation of vorticity with opposite sign to that in the ring (Advaith et al. (2017); Shaw and McHugh (2019); Orlandi and Carnevale (2020)). This process will be particularly intense around temperature inversions, and (16) illustrates that this reduction in the overall circulation of the ring will have an effect on its rate of radial growth (Turner (1960); Meng (1978)).

Although (16) shows that the rate of entrainment of buoyant vortex rings can change if either the circulation or the buoyant content vary, in systems where the baroclinic generation of vorticity due to density gradients is the sole source of circulation, the two will be related. For simple geometries, like a spherical bubble, it is possible to describe the formation of the ring in terms of nondimensional quantities (Walters and Davidson (1962, 1963)) and thus obtain values of the entrainment parameter that are independent of the scale of the system. That would be approximately the case for a nuclear burst occurring in the air and away from the ground, where the fireball is likely to be almost spherical and to evolve in a manner similar to a low density bubble. In other configurations, the interaction of the fireball with its surroundings will make its shape different from spherical, and additional sources of vorticity could also be present, such as those resulting from the interaction with shock waves reflected from nearby structures. All these factors will have an effect on the circulation and vorticity distribution in the ring (Moresco et al. (2014); Lai et al. (2015)), making the entrainment parameter dependent on the emplacement of the weapon.

The association of buoyant vortex rings with thermals provides a physical basis for the entrainment hypothesis that still has not been fully exploited (Lecoanet and Jeevanjee (2019)). The possibility of using (16) to determine the entrainment parameter in terms of the physical properties of a particular configuration would render the model (2)–(5) more robust and extend its applicability to a wider range of scenarios. Although the simplicity of this system is attractive from a computational perspective, this approach is based on an integral description of the cloud, without resolving its internal structure. This can be a shortcoming, such as when describing the interaction of a condensed phase with the cloud, which has important consequences in the final distribution of fallout particles. The intention here is to make further use of the properties of buoyant vortex rings to develop a model that provides a description of the nuclear cloud with greater physical detail, while keeping computational costs commensurate with those of models based on Taylor's description.

While the ability to resolve the evolution of the nuclear cloud without recourse to ad hoc parameterizations and restrictive physical approximations is a naturally desirable aim, obtaining solutions of the general equations of motion for the wide range of scales involved still requires high end computers and the use of parallelization and adaptive mesh refinement techniques. Although the dimensions of the cloud are commensurate with those of atmospheric flows at the convective/meso scales, many of the approximations on which models of the atmosphere are based are not compatible with the type of perturbation that a nuclear explosion introduces. For example, the large variations in characteristic Mach numbers during cloud rise often make it necessary to use separate compressible and incompressible solvers at different stages of the computations (Kanarska et al. (2009)). These additional restrictions on the numerical techniques lead to further difficulties, such as limits in the size of the time steps in the calculations and excessive numerical dissipation (Thornber et al. (2008)). Progress has been made in recent years in the development of solvers with good characteristics for a wide range of compressibility conditions (Munz et al. (2020)), but difficulties remain and this approach is still restricted to research environments, with limited use in operational settings.

The main purpose of this work is to develop a formulation of the nuclear cloud that is intermediate in computational cost to the models based on the entrainment paradigm and those involving a full solution of the equations of motion. Our approach selects a series of approximations that reduces the complexity of the model while maintaining the ability to resolve some of the features of interest. As a result we obtain a description that is suitable for implementation in the type of computer platforms routinely used in operational settings, while providing results within time frames compatible with activities such as emergency response and the collection of samples for forensic analysis.

Our central assumption is that during most of the cloud evolution the main features of the flow can be described in terms of a buoyant vortex ring. This approximation introduces a set of constraints (Shariff and Leonard (1992)) that reduces the number of degrees of freedom of the system and lowers computational costs in comparison to the determination of a general solution of the equations of motion. The use of a vortex ring model to describe atmospheric thermals was pioneered by Levine (1959), who assumed that the vorticity distribution corresponded to that of the so called Hill's vortex (Hill (1894)). In that case, the vorticity is uniform and contained in a spherical region that coincides with the volume of fluid moving with the ring.[‖] Levine (1959) ignored the entrainment process and radial growth of the ring, although this limitation was later remediated by Turner (1964). In contrast to the characteristics of Hill's vortex, the records from nuclear tests show that the vorticity in the ring tends to be contained in a torus with a cross section that is small compared to the ring radius, suggesting that a description based on the assumption of a ring with concentrated vorticity (Lamb (1932)) would be more suitable in this case, and this is the premise we follow here.

To further reduce computational costs, we employ a description of the ring flow based on the vorticity field, making it possible to focus computational resources into the small regions where most of the vorticity is located. We adopt a discretization in terms of vortex elements that reduces the equations describing the evolution of the vorticity field to a set of ordinary differential equations, thus introducing additional numerical advantages. We also assume that the vortex ring remains axisymmetric and swirl free at all times. Despite of this restriction, by combining the velocity field induced by the ring to that of the atmospheric winds it is possible to obtain a 3D velocity distribution that approximates the transport by the nuclear cloud of scalar quantities, such as water vapor mixing ratio and potential temperature, as well as a condensed phase, such as a Lagrangian particle representation of fallout. The combination of these approximations and the numerical approaches described below results in a scheme that has moderate computational requirements but is still able to resolve important features of fallout formation and transport, such as the distribution of particles with different characteristics throughout the cloud and the effects of water condensation and the release of latent heat on the evolution of the cloud.

The approximations in the model and details of its implementation are described below. In Section 2 we summarize the main components of buoyant vortex rings in stratified environments from the point of view of the vorticity field, namely the core of the ring and the vortex sheet resulting from the density gradients between the ring and the surrounding atmosphere. In Section 3 we describe the use of a vortex method to discretize the vorticity field and reduce the dimension of the problem. The determination of the parameters in the model from the yield and emplacement of a nuclear weapon are discussed in Section 4, where we also include example calculations and comparisons with measurements taken from nuclear test records. The approximations on which the model is based and directions for further development are discussed in the Conclusions.

[‖] Hill's (1894) model is many times adopted to describe vortex rings, irrespectively of the vorticity distribution, because of the availability of an analytical expression for the stream function, which reduces the cost of the computations.

2. VORTICITY DESCRIPTION

Under the assumption that the flow is axisymmetric and in a cylindrical frame of reference moving with the ring, the only non-zero component of the vorticity field is in the azimuthal direction, and it is possible to define a Stokes stream function (Lamb (1932)) with streamlines having the characteristics shown in Figure 2. In nuclear clouds, most of the vorticity tends to be concentrated in an annulus or *core* of the ring, while there is also a volume of mainly irrotational fluid moving with it that we will call the *bubble*. In this frame of reference, the surface of the bubble corresponds to the zero streamline.**.

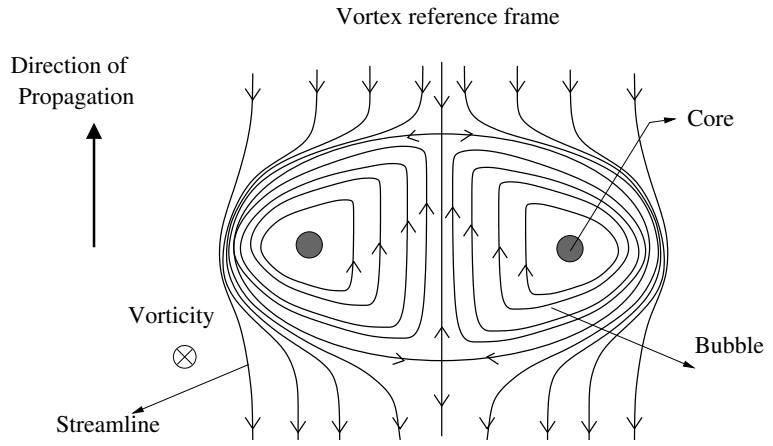

Figure 2. Schematic of the flow streamlines in a frame of reference moving with the vortex ring. The vorticity in the core is in the direction perpendicular to the plane of the figure.

The vorticity in the core is generated during the formation of the ring and its total amount (circulation) and spatial distribution depend on the details of the formation process. In the case of nuclear clouds the density gradients between the fireball and the air around it drive the production of vorticity by the baroclinic mechanism (Batchelor (1967)), which in turn causes the "roll-up" of the fireball into a vortex ring. Depending on the emplacement of the weapon, the core of the ring will contain part or all of the high temperature and low density gases generated during the energy release (Figure 3).

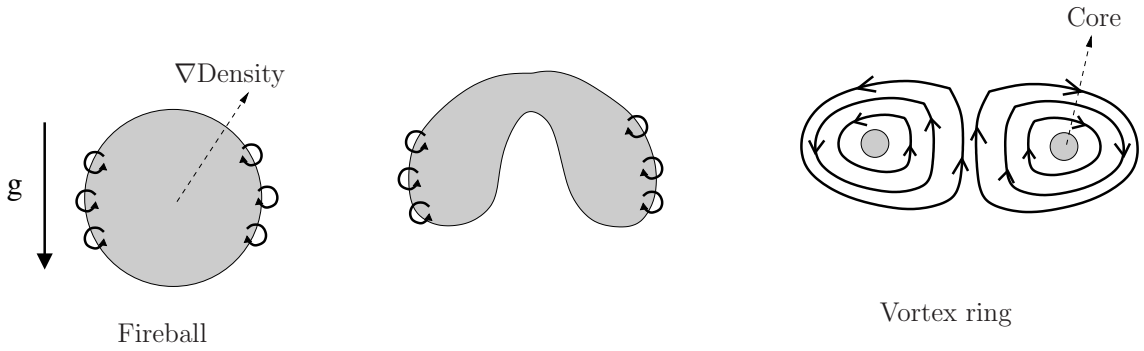

Figure 3. Depiction of the evolution of the fireball (a), through the roll-up processes driven by buoyancy (b) into a vortex ring (c).

**For an unsteady ring the shape of the dividing streamline depends on which definition of vorticity centroid is adopted.

Relations (6)–(14) derived for buoyant vortex rings in the Introduction, also apply to the case where the buoyant fluid is restricted to the core of the ring. In this case, the temporal radial growth of the core as described by (13) results in a change in the shape and volume of the bubble. This entrainment of environmental fluid makes the density of the bubble dependent on that of the atmosphere around it, and in stratified environments, this causes non-zero density gradients between the bubble and the surrounding air. A similar process has been studied in the context of aircraft wakes, where the vorticity distribution is approximated by a vortex pair instead of a ring (Crow (1970); Scorer and Davenport (1970); Spalart (1996); Garten et al. (1998)). Research on aircraft wakes has shown that the vorticity distribution generated as a result of the density gradient between the bubble and its environment is well described by a *vortex sheet* (Hill (1975); Scorer and Davenport (1970)), which is a surface the tangential velocity is discontinuous across (Batchelor (1967)).

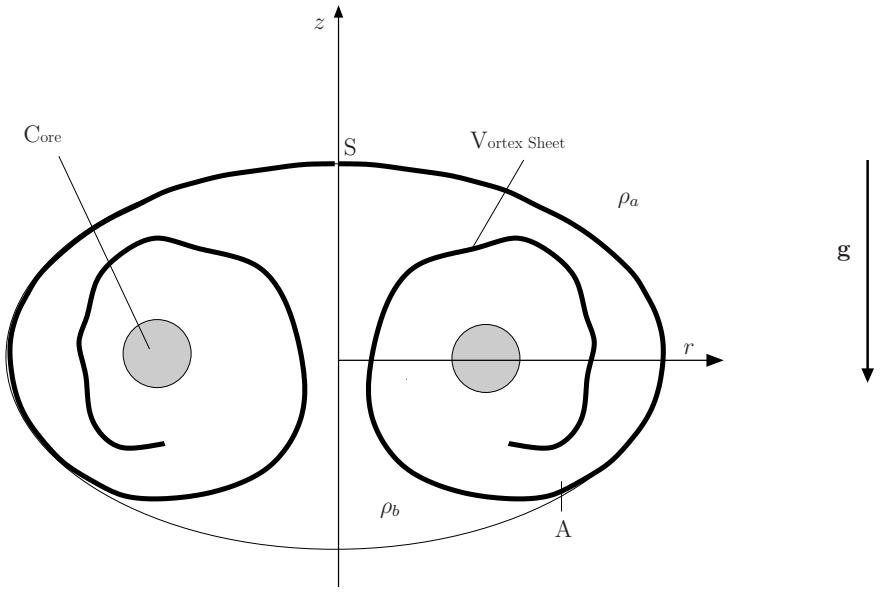

Figure 4. Main components of the vorticity distribution in the vortex ring: the core and vortex sheet.

In our model of the nuclear cloud we will also describe the vorticity generated around the envelope of the ring in terms of a vortex sheet, as shown schematically in Figure 4. We approximate the surface of the bubble as the interface between two immiscible fluids with different densities, which are taken to be uniform inside the bubble (ρ_b) and in the atmosphere around it (ρ_a). This approximation substantially reduces the computational complexity and is valid under the assumptions that the entrained air is well mixed with that of the bubble and that environmental stratification scales are large in relation to the ring dimensions.

The model proposed assumes that the main characteristics of the evolution of the nuclear cloud can be described in terms of these two components: the core of the ring and the vorticity sheet, thus neglecting other sources of vorticity in the flow. Those two regions are where most of the vorticity is concentrated, suggesting that a description in terms of the vorticity field can result in an efficient numerical scheme, with the computation of the velocity field being performed only in the regions of interest, such as at the location of particles representing the condensed phase.

2.1 VORTICITY FIELD

In general terms, a smooth velocity field can be written as the sum of a solenoidal component, determined by the vorticity distribution; an irrotational field, which is a function of the local rate of expansion; and a field that is both solenoidal and irrotational and is determined by the boundary conditions (Batchelor (1950)). In this model we will ignore the second contribution, and we will consider only simple geometries and boundary conditions, resulting in a velocity field that can be determined solely by a localized vorticity distribution. In this context, mass conservation can be imposed by requiring a solenoidal velocity field, usually called an incompressible flow approximation, which results in substantial reductions in computational costs.

For convective flows, the incompressibility condition is associated with the so-called Boussinesq or shallow convection regimes (Batchelor (1953); Spiegel and Veronis (1959); Ogura and Phillips (1962); Dutton and Fichtl (1969); Turner (1973); Gray and Giorgini (1976)). The following conditions are necessary for this approximation:

1. Density and pressure fields can be expressed as small perturbations of a steady state.
2. The fluid motion is confined to a layer of thickness much smaller than the smallest of the scale heights associated to the base state (for example, typically 8 km for the density scale height).
3. The time scale of the flow is of the order of the Brunt–Väisälä time scale (approximately of the order of 100 seconds).
4. The effects of pressure perturbations on the buoyancy force are neglected (as shown by Mahrt (1986), this is equivalent to requiring Froude numbers smaller than one).

In simple terms, the Boussinesq approximation includes the effects of density perturbations only in the buoyancy force term, neglecting their influence on the inertial terms. As a result, in this approach vorticity is only generated baroclinically, and additional sources due to the interaction of density variations with the flow acceleration are not included (Shirgaonkar and Lele (2006)). It has been shown that, even when the scales of the motion are not small and condition 2 is not strictly satisfied, satisfactory descriptions of the evolution of convective flows can be obtained by describing the fluid in terms of potential densities (Spiegel and Veronis (1959); Turner (1973); Yih (1965)).

It is clear that these assumptions are incompatible with the characteristics of nuclear clouds, where the initial temperature differences and pressure fluctuations are substantial. Although the restriction on the scale of the motion (condition 2) could be relaxed by using, for example, a full anelastic approximation (Lipps and Hemler (1982); Won and Lee (2020)), the regimes of validity implied by the other restrictions still will not be met during part of the cloud evolution.

With the aim of obtaining a model that captures the large scale motions in the cloud while keeping computational cost low, we do not look for a solution of the general equations of motion but follow a different approach. Here we will not consider the initial evolution of the density perturbation into a vortex ring, where compressibility effects are important, but instead we take the ring as the initial condition. The trajectory of the core will not be calculated by taking into account the local effects of buoyancy forces and solving the equations of motion directly, but instead it will be based on the assumption that it remains an axisymmetric vortical structure with a circular cross section that can be represented by a buoyant vortex tube. As explained below, and corroborated by the experimental observation of the constancy of the ring

circulation, the description of the core in terms of integral quantities such as its buoyant content gives a good description of its evolution.

In the case of the bubble, and because of the rapid entrainment of ambient air, the density differences between the fluid in its interior and around it will be small and commensurate with those occurring naturally in the atmosphere. Assuming that pressure equilibration between the ring and the atmosphere occurs at a faster time scale than that associated to the motion of the ring, the Boussinesq conditions will apply locally at the interface between the bubble and its environment and will be used to compute the evolution of the vortex sheet.

For the nuclear cloud as a whole the errors incurred by assuming the Boussinesq approximation can be expected to increase with the yield of the weapon and will stem from violations of the constraints associated with the perturbation of the base steady field and the temporal and spatial scales of the motion. The model adopted here is then intended primarily for nuclear clouds originating in bursts with yields in the kiloton range, where the cloud will tend to be confined to the troposphere. In explosions of higher energy, vortex rings are known to remain the dominant feature, but compressibility effects will play an increasing role beyond the initial ring formation period (Moore (1985); Baird (1987)).

If L is the characteristic length of the flow and ν the kinematic viscosity of the fluid, the characteristic time for viscous diffusion will be of the order of L/ν^2. In the case of nuclear clouds, this ratio is much larger than the characteristic time of the flow evolution, and an inviscid approximation in terms of Euler's equations is valid (Liepmann and Roshko (1985)). These conditions can also be described as a high Reynolds number regime (Batchelor (1967)). For an incompressible isentropic flow, satisfying the ideal gas equation of state, the equations of motion can be written (Turner (1973)):

$$\frac{\partial \rho}{\partial t} + \boldsymbol{u} \cdot \nabla \rho = 0, \tag{17}$$

$$\rho \frac{D\boldsymbol{u}}{Dt} = \rho \left(\frac{\partial \boldsymbol{u}}{\partial t} + \boldsymbol{u} \cdot \nabla \boldsymbol{u} \right) = -\nabla p + \rho \, \mathbf{g}, \tag{18}$$

$$\nabla \cdot \boldsymbol{u} = 0, \tag{19}$$

where p is the pressure, $\boldsymbol{u}$ is the velocity, ρ is the potential density, $\mathbf{g}$ is the gravitational acceleration, and t represents time. The potential density is defined from the standard density ($\rho*$) by means of the Exner function Π

$$\rho = \rho^* \Pi, \quad \Pi = \left(\frac{p}{p_0} \right)^{R_g/c_p}, \tag{20}$$

where p_0 is a reference pressure, R_g is the gas constant, and c_p is the specific heat capacity at a constant pressure. [††]

We will limit ourselves to the case when the flow is at rest at infinity and contained in a half-space limited by a flat boundary, where we impose the condition

$$\boldsymbol{u} \cdot \boldsymbol{n} = 0, \tag{21}$$

where $\boldsymbol{n}$ is the normal to the boundary. By imposing only this boundary condition we are neglecting the development of boundary layers and the associated sources of vorticity.

[††] In the examples discussed in Section 4.3 p_0 was taken as the pressure at the height of burst.

Taking the curl of (18) we obtain an equation for the vorticity $\boldsymbol{\omega}$,

$$\frac{D\boldsymbol{\omega}}{Dt} = -\nabla \times \left(\frac{1}{\rho}\nabla p\right), \tag{22}$$

where we have omitted the so called vortex stretching term ($\boldsymbol{\omega} \cdot \nabla \boldsymbol{u}$) because of the axisymmetry of our configuration. The right hand side of (22) represents the baroclinic generation of vorticity at a rate proportional to the local gradients of pressure and density. For buoyant vortex rings, this mechanism is important in the vicinity of the core and the surface of the bubble.

In our model we assume that the circulation of the core remains constant and given by the initial conditions, and we only compute the sources of vorticity associated with the surface of the bubble, where the density gradients can be considered to be small and the Boussinesq applicable. In a frame of reference moving with the ring, we will then assume that p and ρ outside the core can be decomposed into reference states, described by $\bar{p}$ and $\bar{\rho}$, plus perturbations p' and ρ',

$$p = \bar{p} + \eta p', \tag{23}$$

$$\rho = \bar{\rho} + \eta \rho', \tag{24}$$

with $|\eta| \ll 1$. Taking the reference state to be in (irrotational) hydrostatic equilibrium,

$$\nabla \bar{p} = \bar{\rho}\mathbf{g}, \tag{25}$$

to order η we can write

$$\frac{D\boldsymbol{\omega}}{Dt} = \frac{\nabla \rho'}{\bar{\rho}} \times \mathbf{g} + \frac{1}{\bar{\rho}^2}\nabla \bar{\rho} \times \nabla p'. \tag{26}$$

As shown by Ogura and Phillips (1962) and Lipps and Hemler (1982), $\nabla p'$ is a factor η smaller than ρ' and the second term on the right hand side can be neglected to order η giving

$$\frac{D\boldsymbol{\omega}}{Dt} = \frac{\nabla \rho'}{\bar{\rho}} \times \mathbf{g}. \tag{27}$$

2.2 VORTEX SHEET EVOLUTION

Vortex sheets are an idealization used to describe a variety of inviscid flows, such as shear and mixing layers, where the vorticity distribution is approximated by a surface, to which the vorticity vector is tangent. They can arise in homogeneous fluids as the wake of obstacles with a sharp trailing edge (Prandtl and Tietjens (1934)) or at the interface between two immiscible fluids with different densities, where vorticity is generated by the baroclinic mechanism (Sohn (2004)).

The vortex sheet is characterized by the continuity of the normal component of the velocity vector and a jump in the tangential component. If $\boldsymbol{u}_1$ and $\boldsymbol{u}_2$ represent the velocity vectors at each side of the sheet, these conditions are

$$\boldsymbol{u}_1 \cdot \tilde{\boldsymbol{n}} = \boldsymbol{u}_2 \cdot \tilde{\boldsymbol{n}}, \tag{28}$$

and

$$\boldsymbol{\gamma} = (\boldsymbol{u}_1 - \boldsymbol{u_2}) \times \tilde{\boldsymbol{n}}, \tag{29}$$

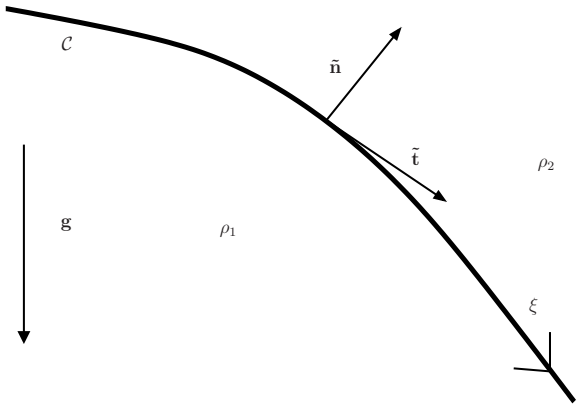

Figure 5. Parameterization of an axisymmetric vortex sheet separating fluids with densities ρ_1 and ρ_2.

where $\tilde{\boldsymbol{n}}$ is the normal to the sheet. The magnitude of the vector $\boldsymbol{\gamma}$ is called the strength of the sheet and in the axisymmetric case is equal to the jump in tangential velocity

$$\gamma = |\boldsymbol{\gamma}| = (\boldsymbol{u}_1 - \boldsymbol{u_2}) \cdot \tilde{\boldsymbol{t}}, \tag{30}$$

where $\tilde{\boldsymbol{t}}$ is the tangent to the sheet (Pozrikidis (2000)).

In terms of the vorticity field $\boldsymbol{\omega}$ we can also write

$$\boldsymbol{\omega}(\boldsymbol{r}, t) = \boldsymbol{\gamma}(\boldsymbol{r}(t))\delta(\tilde{n}), \tag{31}$$

where $\tilde{n} = |\tilde{\boldsymbol{n}}(t)|$ and $\delta(\cdot)$ is the Dirac delta function.

Vortex sheets are subject to the Kelvin–Helmholtz instability (Saffman and Baker (1979); Meiron et al. (1982)) and following their detailed evolution for long periods of time is computationally expensive because of the many spatial scales involved. Instead, our aim here is to resolve the sheet qualitatively, putting an emphasis in capturing the rate of production of vorticity on the surface of the bubble as this will impact the total circulation and stability of the ring.

Computing the evolution of a vortex sheet separating two fluids with different densities requires calculating at each point on the sheet the velocity induced by the rest of the sheet and the variation in the strength with time. In the axisymmetric case, the sheet can be described as a curve $C = r(\xi)$ on a meridional plane and parameterized in terms of a scalar ξ (Figure 5). The velocity at point $\boldsymbol{r}$ generated by the sheet can then be expressed as (Kaneda (1990); Caflisch and Li (1992))

$$\boldsymbol{u}_s(\boldsymbol{r}, t) = \frac{1}{4\pi}\mathrm{PV}\int_C \boldsymbol{\gamma}(\boldsymbol{r}(\xi, t)) \times \frac{\boldsymbol{r}(t) - \boldsymbol{r}(\xi, t)}{|\boldsymbol{r}(t) - \boldsymbol{r}(\xi, t)|^3} d\xi, \tag{32}$$

where PV denotes principal value and the integrals are taken over the length of the sheet.

In the Boussinesq limit and taking the fluid densities on each side of the sheet to correspond to $\bar{\rho}$ and $\bar{\rho} + \rho'$, with $|\rho'| \ll \bar{\rho}$, the analysis in the previous section in combination with (31) shows that the strength at a point $\boldsymbol{r}$ on the sheet satisfies (Baker et al. (1982); Sohn (2004); Chang and Llewellyn Smith (2020))

$$\frac{D\gamma}{Dt} = \frac{\rho'}{\bar{\rho}}\mathbf{g} \cdot \tilde{\boldsymbol{t}}. \tag{33}$$

In this model of the vortex ring, the motion of the sheet is determined by contributions from the self-induced velocity obtained by applying (32) to points on the sheet, plus an additional contribution from the core of the vortex ring. As shown schematically in Figure 4, as a result of the radial growth of the core and the entrainment process, the vorticity generated on the surface of the bubble tends to be entrained into the ring, resulting in a sheet with a complex structure. Describing this process in full detail is beyond the level of fidelity of this model; our main objective here is to approximate the rate of production of vorticity due to atmospheric stratification and it will then be assumed that vorticity is generated only on the most external section of the sheet, approximately along the length between the points S and A in Figure 4.

2.3 CORE DESCRIPTION

The core of the vortex ring is where most of the vorticity is initially concentrated, and it is the main driver of the flow during the majority of the cloud evolution. During the roll-up phase of the fireball, its surface evolves into a toroidal shape for which the net production of vorticity by the baroclinic mechanism is zero (Figure 3(b)). Although from this point the circulation in the core remains approximately constant, vorticity of both signs continues to be produced at different points of its interface with the bubble and, as described below, this drives the radial growth of the ring.

As shown schematically in Figure 6, the variation in direction of the density gradients at different points on the surface of the core (c.f., $\nabla\rho_1$ and $\nabla\rho_2$) results in the production of vorticity of opposite signs along the exterior and interior (closer to the axis of symmetry) surfaces of the core. This constant production and destruction of vorticity causes a displacement of the vorticity centroid toward larger radii and the increase in volume of the bubble, leading to the entrainment of ambient fluid (Zhao et al. (2013); McKim et al. (2020)). An alternative way of understanding this process is by following a fluid particle as it moves along the surface of the core from the point P in Figure 6. Its velocity of motion would be of the order of Γ_c/ϵ, where Γ_c is the core circulation and ϵ the distance from the centroid of vorticity. The particle will first experience an increase in its circulation followed by a decrease, as it moves along the zones of production and destruction of vorticity. This will result in a local excess of vorticity $\Delta\Gamma_c$ around the upstream (rear) part of the core, as indicated in Figure 6, which will induce a radial velocity on the vorticity centroid of the order of $\Delta\Gamma_c/\epsilon$. According to (22), the magnitude of $\Delta\Gamma_c$ produced baroclinicly will be proportional to the density gradient between the core and the bubble (i.e., the buoyant content of the core) and inversely proportional to its circulation, because the larger the circulation the more rapidly the fluid moves around the boundary. If r_c and z_c are the radial and axial coordinates of the vorticity centroid and using (15)

$$\frac{dr_c}{dz_c} = \frac{dr_c}{dt}\frac{dt}{dz_c} \sim \frac{\Delta\Gamma_c}{\epsilon}\frac{r_c}{\Gamma_c} \sim \frac{B_c}{\Gamma_c^2}, \tag{34}$$

with

$$B_c = V_c\frac{\rho_c - \rho_b}{\rho_b}g, \tag{35}$$

where B_c is the buoyant content and V_c the volume of the core, respectively. This relation is equivalent to (16) applied to the core of the ring but now obtained by taking into account the details of the vorticity generation mechanism.

We will assume that the density of the bubble can be written $\bar{\rho}_b + \Delta\rho_b$, where $\bar{\rho}_b$ is the initial value and $\Delta\rho_b$ accounts for the changes during the entrainment process due to the stratification of the atmosphere. If we

take those changes to be small in comparison to the density gradient between the core and the bubble,

$$\left| \frac{\Delta\rho_b}{\rho_c - \bar{\rho}_b} \right| \ll 1, \tag{36}$$

the buoyant content of the core will remain approximately constant during the evolution of the ring.

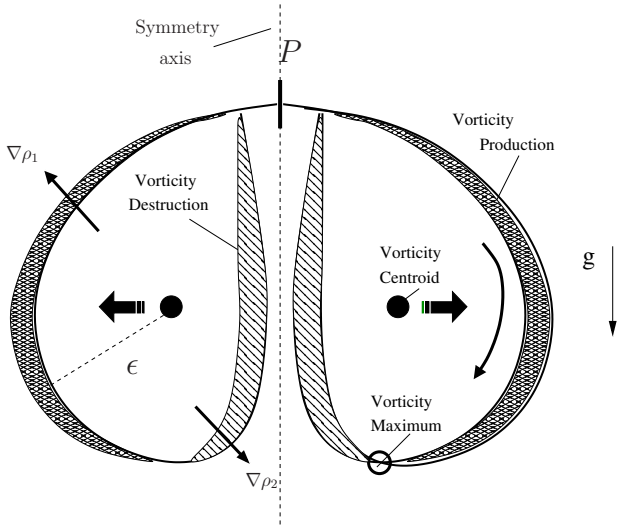

Figure 6. Schematic representation of the variations in baroclinic production of vorticity around the surface of the core.

Given the large density gradients and flow velocities in the proximity of the core, the Boussinesq or anelastic approximations are not applicable, and resolving the flow in detail, including changes in the distribution of vorticity, is beyond the level of detail of the model presented here. Instead we describe the core by means of an axisymmetric vortex tube (Batchelor (1967)) subject to a buoyancy force. By this approximation we are neglecting details of the core evolution, such as rapid oscillations around the mean motion, which have been shown to be higher order perturbations to the trajectory obtained from the type of model adopted here (Moffat and Moore (1978); Pozrikidis (1986); Lundgren and Mansour (1991)). Here the effects of the vorticity distribution on the dynamics of the core will be taken into account by selecting the function $\mathcal{F}(\omega)$ in the expression for the self-induced velocity (15). We will further assume that the cross section of the core is circular with radius ϵ, which will be taken to be small compared to the radius of the ring.

Lundgren and Mansour (1991) proposed a model of a slender (thin core) buoyant vortex tube, in which the radial (u) and axial (v) velocity components in a frame of reference moving with the velocity given by (15) satisfy

$$V_c \frac{dv}{dt} = -2\pi r_c \Gamma_c u + B_c. \tag{37}$$

The first term on the right hand side of this relation corresponds to the contribution of the Kutta–Joukowski force, a form of lift resulting from the circulation in the core and the flow around it (Widnall and Bliss (1971)). It is possible also to add a drag force component to this equation, but given the high Reynolds

number of the flow, it can be expected to be a small contribution (Gan et al. (2012)), and it will be neglected here.*

Ignoring inertial forces, (37) reduces to

$$2\pi r_c \Gamma_c u = 2\pi r_c \Gamma_c \frac{dr_c}{dt} = B_c, \tag{38}$$

which when rearranged gives

$$\frac{dr_c}{dt} = \frac{B_c}{2\pi\Gamma_c}\frac{1}{r_c}, \tag{39}$$

and agrees with (13). This is equivalent to making a quasi-steady approximation, where it is assumed that the instantaneous forces are equivalent to those for steady motion at the same instantaneous velocity and radius. Based on this buoyant vortex filament description, Lundgren and Mansour (1991) explained the radial growth of the ring as required to balance the upward buoyancy force with a downward lift.

For a non-buoyant ring in steady motion with a thin core, the self-induced velocity of propagation of the ring can be written as (Tung and Ting (1967))

$$\frac{dz_c}{dt} = \frac{\Gamma_c}{r_c} f(\epsilon/r_c), \tag{40}$$

and expressions for $f(\epsilon/r_c)$ have been obtained as expansions in (ϵ/r_c) for specific vorticity distributions. In general, the self-induced velocity of propagation of the core can be written in the form (Hicks (1884); Lamb (1932); Saffman (1970); Fukumoto and Moffatt (2008); Meleshko et al. (2012))

$$\frac{dz_c}{dt} = \frac{\Gamma_c}{4\pi r_c}\left[\ln\frac{8r_c}{\epsilon} + A - \frac{1}{2} + o\left(\frac{\epsilon}{r_c}\right)\right], \tag{41}$$

with $A = 1/4$ in the case of uniform vorticity (ω/r constant) and $A = 0$ for a hollow vortex. Here we will assume the distribution of vorticity in the core to be uniform. Continuous descriptions of the family of vortex rings with vorticity distributions ranging from the thin core limit to Hill's vortex model are also available (Fraenkel (1970, 1972); Norbury (1973), but their use here would increase the computational costs and not enough experimental data are currently available to validate their applicability to the nuclear cloud. In the case of buoyant vortex rings, the motion is not steady, but we will assume that an expression of the form (41) applies instantaneously and we will take the slender ring approximation to be valid throughout the evolution of the cloud, even if at early time the ratio ϵ/r_c could be of order one.

To fully describe the dynamics of the core, (39) and (41) need to be combined with an equation for the core radius ϵ, which will also permit the calculation of the bubble boundary for the computation of the vortex sheet. When describing the evolution of the vortex ring in a stratified medium, the mutual interaction between the vortex sheet and the core need to be taken into account, which will result in additional contributions to the velocity field that each of these components will experience.

*In other models of the nuclear cloud the drag force is needed to represent the differences in flow characteristics between a vortex ring and a buoyant fluid parcel (Morrison and Peters (2018)). Since our model is based on a vortex ring description explicitly, it is not necessary to include this additional force contribution.

3. VORTEX METHOD

In fluid systems that can be described in terms of localized regions of vorticity surrounded by potential flow, *vortex methods* are techniques that solve the equations of motion by using a discretization of the vorticity field. In this approach, the original partial differential equations are replaced by a finite set of ordinary differential equations describing the trajectories of individual vortex elements. For high Reynolds number flows, this Lagrangian approach offers a grid-less description that avoids problems such as numerical diffusion and the need to resolve convective derivatives, characteristic of Eulerian schemes (Leonard (1980)). The velocity field generated by vortex methods has been proven to converge to the real velocity field of an incompressible and inviscid fluid when there are no boundaries and the vorticity is localized (has compact support) (Hald and Prete (1978); Hald (1979); Beale and Majda (1982a,b)).[†]

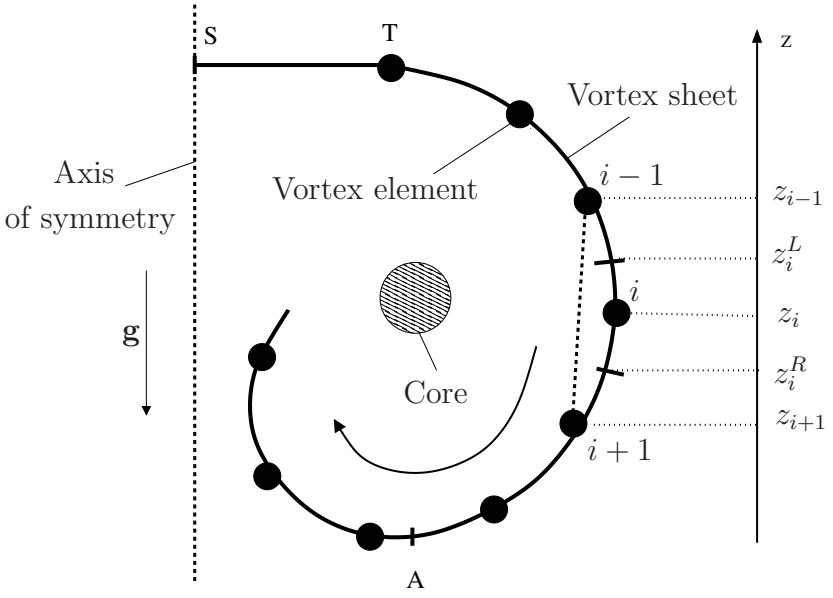

Figure 7. Discretization of the vortex sheet on the surface of the bubble by vortex elements. The figure corresponds to a section of the sheet in a meridional plane of the vortex ring.

Here we will use a discrete vortex approximation to describe the vortex sheet that develops on the surface of the bubble of the vortex ring in a stratified medium. Rosenhead (1931) was the first to propose the computation of the motion of vortex sheets in 2D flows by means of a discretization in terms of point vortices, each containing the circulation corresponding to a segment of the sheet. The equivalent description in 3D axisymmetric flows can be carried out using coaxial circular vortex filaments as vortex elements (Acton (1980); Nitsche (2001)). Through this discretization, the vortex elements are considered to be an approximation to the vortex sheet, which can then be reconstructed by an interpolation procedure, as shown schematically on a meridional plane in Figure 7 (c.f., Figure 4), and the velocity induced by the whole sheet is then obtained from the sum of the contributions of each vortex element. This method can be interpreted also as a trapezoidal quadrature scheme for the principal value of the integral in (32), with one vortex element associated with each interval of the sheet.

[†]Extensions of the vortex methods to compressible (Sod (1991); Nitsche and Strickland (2002); Eldredge et al. (2002)) and viscous (Chorin (1973); Baden and Puckett (1990)) flows have also been developed.

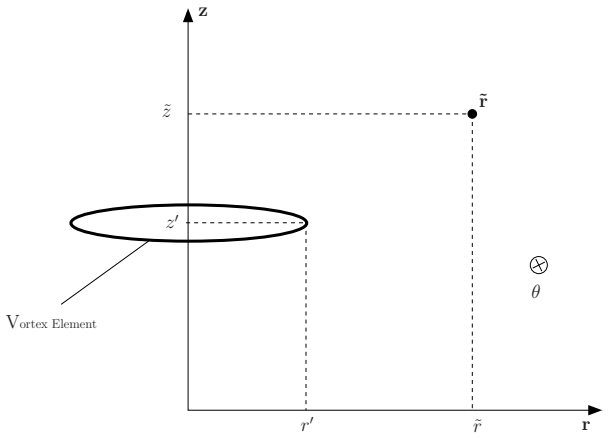

Figure 8. Cylindrical coordinate system used in the description of the stream function corresponding to a circular vortex filament.

For a circular vortex filament in an infinite domain, it is possible to define a Stokes stream function, from which the components of the velocity can be obtained by differentiation. We will use cylindrical coordinates (r, θ, z), with z denoting the position along the axis of symmetry, r denoting the radial, and θ the azimuthal coordinates (Figure 8). On a meridional plane, then the Stokes stream function at a point $(\tilde{z}, \tilde{r})$ due to a filament with circulation $\tilde{\Gamma}$, radius r' and center axial coordinate z' is given by (Lamb (1932))

$$\psi(\tilde{z}, \tilde{r}\,; z', r', \tilde{\Gamma}) = \frac{\tilde{\Gamma}}{4\pi} \int_0^{2\pi} \frac{\tilde{r} r' \cos\theta}{[(\tilde{z} - z')^2 + \tilde{r}^2 + r'^2 - 2\tilde{r} r' \cos\theta]^{1/2}} d\theta, \tag{42}$$

and the velocity has radial (u) and axial (v) components:

$$u = -\frac{1}{\tilde{r}} \frac{\partial \psi}{\partial \tilde{z}}, \quad v = \frac{1}{\tilde{r}} \frac{\partial \psi}{\partial \tilde{r}}. \tag{43}$$

Relation (42) can also be written as (Lamb (1932))

$$\psi(\tilde{z}, \tilde{r}\,; z', r', \tilde{\Gamma}) = \frac{\tilde{\Gamma}}{2\pi} (R_1 + R_2)[F(\lambda) - E(\lambda)], \tag{44}$$

where $\lambda = (R_2 - R_1)/(R_2 + R_1)$, $R_1^2 = (\tilde{z} - z')^2 + (\tilde{r} - r')^2$, $R_2^2 = (\tilde{z} - z')^2 + (\tilde{r} + r')^2$, and $F(\lambda)$ and $E(\lambda)$ are the complete elliptic integrals of the first and second kind, respectively. This second expression for ψ is more convenient from a numerical perspective because approximations to F and E are readily available, such as in terms of series of Chebyshev polynomials (Cody (1965)).[‡]

The early application of vortex methods to the evolution of vortex sheets revealed the appearance of a singularity in finite time at which the curvature diverges (Moore (1979)). This has been associated to the fact that vortex sheets are a mathematical idealization of real flows and to the singularity in the integrand in (32) for points on the sheet. Chorin and Bernard (1973) showed that it is possible to compute the motion using vortex methods past the singularity formation by introducing a smoothing parameter into the governing equations to regularize the flow. When this approach is followed in two dimensions, the vortex elements are usually called vortex blobs (Leonard (1980)).

[‡]The derivatives in (43) can also be expressed in terms of the complete elliptic integrals $F(\lambda)$ and $E(\lambda)$ (Nitsche and Krasny (1994)).

The approaches that have been proposed to introduce a desingularization of vortex sheets may be divided roughly into two classes: those that seek to incorporate physical aspects, such as the finite thickness of the sheet (Baker and Shelley (1990)), and those driven solely by numerical considerations (Krasny (1986a)). The latter approach is usually more economical from the computational standpoint and will be followed here, although in this case it is not possible to link the regularization parameter to spatial dimensions of the sheet.

In the most common vortex sheet regularization, the singular Biot–Savart kernel in (42) is replaced by its convolution with an algebraically decaying smooth function. Following this approach, Krasny (1986a,b) proposed the following expression for the stream function:

$$\psi(\tilde{z},\tilde{r}\,;z',r',\tilde{\Gamma}) = \frac{\tilde{\Gamma}}{4\pi}\int_0^{2\pi} \frac{\tilde{r}r'\cos\theta}{\left[(\tilde{z}-z')^2+\tilde{r}^2+r'^2-2\tilde{r}r'\cos\theta+\delta^2\right]^{1/2}}d\theta, \tag{45}$$

where δ plays the role of a smoothing parameter. Later Tryggvason et al. (1991) showed numerically that, for vortex sheets approximated by vortex blobs, in the limit $\delta\to 0$ the regularized solution is the same as that corresponding to the Navier–Stokes equations when the Reynolds number tends toward infinity. Numerical studies have also shown that decreasing δ results in a more detailed sheet structure, but at the same time, there is an increased chance that round-off errors will trigger instabilities (Krasny (1986a,b, 1987, 1991). In general, for good convergence, the recommended practice is to use values of δ that are larger than the separation between vortex elements, although more sophisticated approaches have also been developed (Cotett et al. (2000)).

We can use relation (33) to calculate the evolution of the circulation corresponding to a section of the vortex sheet, which will be the circulation associated to a vortex element. We will assume that the potential density of the bubble can be written as $\rho_a+\rho_b'$, where ρ_a is the density of the air around the ring and $|\rho_b'/\rho_a|$ is small. If the end points of the section of the sheet associated to vortex element i have axial coordinates z_i^L and z_i^R (Figure 7) corresponding to values of the sheet parameter ξ_i^L and ξ_i^R, respectively, integration of (33) gives the following for the circulation of the element (Γ_i),

$$\frac{D\Gamma_i}{Dt} = \frac{D}{Dt}\int_{\xi_i^L}^{\xi_i^R}\gamma(\boldsymbol{r}(\xi),t)\,d\xi = \frac{\rho_b'}{\rho_a}\int_{\xi_i^L}^{\xi_i^R}\mathbf{g}\cdot\tilde{\boldsymbol{t}}(\xi)\,d\xi = g\,\frac{\rho_b'}{\rho_a}\,(z_i^R-z_i^L), \tag{46}$$

with $g=|\mathbf{g}|$.

In our model we are mainly interested in resolving the rate of vorticity production, which mostly occurs in the portion of the sheet delimited by S (the stagnation point) and A in Figure 7. As a result of the velocity field induced on the sheet by the core of the ring, the vortex elements in this region move as indicated by the arrow, which results in the section of the sheet between S and A being continuously stretched. In vortex methods, the accuracy with which the discretization represents the sheet depends on the density (number and separation) of the vortex elements. Several methodologies with different levels of sophistication have been proposed to determine distributions of vortex elements that maintain the desired level of accuracy as the characteristics of the sheet change with time (Fink and Soh (1978); Meng (1978); DeVoria and Mohseni (2018)). Applying those techniques usually requires periodically computing a smooth approximation to the sheet from the vortex elements, for example by means of a cubic spline, and defining a new set of vortex elements with the desired properties. To avoid this computational cost, here we impose an approximately uniform distribution of vortex elements only in the region of the vortex sheet where vorticity is generated, and this density is maintained by periodically adding new vortex elements between S and the first existing

element along the sheet T (Figure 7).[§] As those elements are transported into the interior of the bubble no further attempt is made to keep them in a uniform distribution, which results in a progressive deterioration of the accuracy of the approximation. Despite this loss of resolution, this approach has been shown to give a satisfactory description of the qualitative aspects of the sheet evolution also in other types of flows (Meng and Thomson (1978)), including mixing (Ashurst (1988)) and shear (Grabowski and Telste (1978)) layers.

The calculation of the variation of the circulation of a given vortex element according to (46) requires assigning to it a section of the curve representing the vortex sheet on a meridional plane. To avoid the numerical cost of interpolation procedures, we follow the approach by Meng (1978)), where the curve is represented by a polygonal chain and the variation of the element circulation is computed as half of that obtained when the integral (46) is applied to the segment defined by the two vortex elements adjacent to the element of interest. In terms of Figure 7, the expression for vortex element i in terms of elements $i-1$ and $i+1$ is given by

$$\frac{D\Gamma_i}{Dt} = g\,\frac{\rho_b'}{\rho_a}\,\frac{(z_{i+1}-z_{i-1})}{2}. \tag{47}$$

The variation in time of the circulation of the whole vortex sheet can then be written

$$\frac{D\Gamma_b}{Dt} = \sum_{i=S\ldots A} \frac{D\Gamma_i}{Dt}, \tag{48}$$

where the sum includes only those vortex elements contained in the section of the sheet between the points S and A where vorticity is generated.

The velocity induced by the sheet at a point $\tilde{\boldsymbol{r}} = (\tilde{z}, \tilde{r})$ can be computed by means of the stream function for the whole sheet ($\psi_s(\tilde{z}, \tilde{r}, t)$), which in turn can be written as the superposition of the stream functions for each vortex element,

$$\psi_s(\tilde{z}, \tilde{r}, t) = \sum_{i}^{N} \psi(\tilde{z}, \tilde{r}\,; z_i, r_i, \Gamma_i), \tag{49}$$

where (z_i, r_i) are the coordinates of element i, $\psi(\tilde{z}, \tilde{r}\,; z_i, r_i, \Gamma_i)$ is obtained from (45), and N is the number of elements representing the sheet. In combination with (43), this results in a discrete approximation to (32).

To describe the core of the vortex ring we also use a circular vortex filament with constant circulation Γ_c and a regularization parameter δ chosen to give a self-induced velocity for the filament that matches the theoretical value of a slender ring with circular core with radius ϵ and a specific vorticity distribution. As discussed by Moore (1971), it is possible to choose a regularization parameter that is proportional to the core radius and gives a self-induced velocity for a particular choice of $\mathcal{F}(\omega)$ in (15). In the case of a hollow vortex it corresponds to $\delta = \exp(-1/4)\,\epsilon$ and for uniform vorticity distribution corresponds to $\delta = \exp(-3/4)\,\epsilon$. We will use the latter expression for the example calculations below.

In the Lagrangian framework of the vortex method, the evolution of the vortex ring is obtained from the self-induced and mutual velocity fields associated with the core and vortex sheet. The velocity of the core can then be written

$$\boldsymbol{u_c} = \boldsymbol{u_c^c} + \boldsymbol{u_c^s}(\boldsymbol{r}_c), \tag{50}$$

[§]The location of the bubble boundary is determined from the zero stream function associated to the core.

where $\boldsymbol{u}_{\boldsymbol{c}}^{c}$ is the self-induced velocity and $\boldsymbol{u}_{\boldsymbol{c}}^{s}$ the component due to the vortex sheet. The former is obtained from (39) for the radial component, and the axial component is obtained from (41). The velocity induced by the sheet on the core is determined from $\psi_s(z_c, r_c, t)$ according to (49).

In the same manner, the motion of the sheet is determined by a contribution due to the core plus that due to the self-induced velocity. The velocity of vortex element i in the sheet corresponds to

$$\boldsymbol{u_i} = \boldsymbol{u}_s^c(\boldsymbol{r}_i) + \boldsymbol{u}_s^s(\boldsymbol{r}_i), \tag{51}$$

where $\boldsymbol{u}_s^c(\boldsymbol{r}_i)$ is obtained using (43) with the stream function (45) evaluated as $\psi(z_i, r_i\,; z_c, r_c, \Gamma_c)$ with the value of δ for the core, and $\boldsymbol{u}_s^s(\boldsymbol{r}_i)$ is given by computing $\psi_s(z_i, r_i, t)$.

Equations (50), (51), and (47) are a set of ordinary differential equations that describe the evolution of the location and circulation of the vortex elements corresponding to the vortex sheet and the core. The approach that is followed to determine the value of ϵ required to compute the velocity induced by the core is related to the stability characteristics of the vortex ring and described in Section 4. Since the generation of vorticity on the sheet was expressed in terms of a mean density for the bubble (ρ_c), it is necessary to provide a mechanism to update this value at each time step. Here we will assume that when ambient air is entrained in the bubble there is no change in volume due to the mixing. Within the level of approximation followed here, the potential density of the bubble can be computed at time $t+1$ in terms of the values at time t with

$$\rho_b^{t+1} = \frac{\rho_b^t V_b^t + (V_b^{t+1} - V_b^t)\rho_a^t}{V_b^{t+1}}, \tag{52}$$

where V_b corresponds to the volume of the bubble and ρ_a^t is a mean ambient fluid density at time t. These values are used at each time step to compute the change in circulation of each vortex element using (47) with $\rho_b' = \rho_b^t - \rho_a^t$. The volume of the bubble is determined from the zero stream function in a frame of reference moving with the core.

In this model we make the approximation that the velocity field induced by the vortex ring is completely determined by the associated vorticity distribution. This can be combined with a 2D (purely horizontal) atmospheric wind profile, by assuming the the ring moves with the external velocity field. In this way it is possible to obtain an approximation to the 3D velocity field in and around the cloud, which can be used to compute, for example, the transport of Lagrangian particles or scalar species in an Eulerian framework. In the latter case, the velocity field can be computed in terms of the stream functions of all the vortex elements (sheet plus core) using expressions like (49) or by first mapping the vorticity from the elements to the Eulerian grid, as is done in the *vortex in cell method* (Tryggvason (1989); Brecht and Ferrante (1990)). In the latter approach, the motion of the vortex elements is also determined from the grid-interpolated vorticity field, which can be more economical than solving (50) and (51), for which the cost will increase as the number of vortex elements squared. Nevertheless, it should be taken into consideration that using this type of mapping also introduces a grid-dependent resolution into the vortex method.

For the simple geometry considered here, the boundary condition (19) can be satisfied by the method of images (Saffman (1992); Milne-Thomson (2011)), where for each vortex element there is one with circulation of the opposite sign located at the location of its mirror image from the boundary. Following this approach, the boundary can be eliminated and the flow obtained in terms of a set of vortex elements in an infinite domain, making possible the use of expression (42) for the stream function and the application of convergence results for vortex methods to this system.

4. STABILITY REGIMES AND SCALING RELATIONS

There are numerous experimental studies of the evolution of vortex rings, although only a few consider the conditions applicable to the nuclear cloud, which is a strongly buoyant core in a stratified medium. Laboratory scale setups are also necessarily restricted to much lower values of the Reynolds number, with viscous effects clearly present in some of the configurations reported. The mechanism used to initiate the flow also has a direct impact on the initial vorticity distribution and the parameters of the vortex ring, which needs to be taken into account when interpreting the results and linking them to the evolution of the nuclear cloud. Both in liquids and gases, the most favored method of generating the vortex ring is by introducing into the main fluid a jet of short duration during which fluid is pushed through an orifice using a piston or a loudspeaker (Glezer and Coles (1990); Widnall and Sullivan (1973)). In this case, the vortex sheet that develops at the border of the orifice rolls up to form the core of the vortex ring, but secondary regions of vorticity also appear that have an effect on the overall circulation of the ring (Didden (1979)). Alternative approaches to generating the ring based on density perturbations, which may be more similar to the way the nuclear fireball evolves, involve releasing a fluid of different density by inverting a hemispherical cup (Scorer (1957); Sanchez et al. (1989); Thompson et al. (2000)) or by piercing a membrane (Bond and Johari (2010); Be Hagh et al. (2015)). Although none of these setups reproduces exactly the conditions of interest, they provide valuable information on the evolution of vortex rings, particularly in terms of their stability properties and transition between different regimes. This information will be used here to gain an understanding of the regimes of validity of the proposed model for the nuclear cloud. Rough estimates of the values of the parameters in the model will be obtained by scaling considerations, with the expectation that additional measurements from laboratory experiments and the re-evaluation of historic records will make it possible to determine those values more accurately in the future.

In the 1950s and 1960s, research on thermals, primarily within atmospheric settings, naturally addressed properties of vortex rings, especially after Turner (1957) highlighted the relation between the two flow descriptions. Those studies focused on validating the similarity relations proposed by Morton et al. (1956), mainly measuring angles of spread and stabilization heights or maximum penetration distances (Scorer (1957); Woodward (1959); Richards (1961); Saunders (1962)). Those initial experimental results were mostly qualitative because of the limited measurement techniques available at the time, usually based on observations of the patterns generated by the transport of passive scalars by the flow. Better characterizations of the vorticity and density fields became possible with the development of more powerful experimental approaches in the 1970s, such as laser-Doppler anemometry (Widnall and Sullivan (1973); Sullivan et al. (1973)), particle image velocimetry (Weigand and Gharib (1994)), and laser-induced fluorescence (Johari (1992)). These techniques offer a nonintrusive way to determine vector fields and density distributions, without introducing the kind of perturbations inherent to other approaches such as hot-wire anemometry (Dziedzic and Leutheusser (1996)). In recent years, it has also become possible to study computationally the early stages of transition to turbulence in vortex rings (Archer et al. (2008); Mao and Hussain (2017)), which has provided an additional insight into the evolution of the flow as the instability progresses.

4.1 VORTEX RING STABILITY

The experimental and numerical evidence indicates that in most configurations, the core of the vortex ring shortly after its formation is laminar (Glezer and Coles (1990)), and this was found to especially be the case for buoyant vortex rings, where density gradients can act as a stabilizing mechanism (Turner (1957)). Experimentally it has been observed that during the time the core remains laminar, little mixing happens

between the fluid in it and that in the bubble (Vladimirov and Tarasov (1979); Maxworthy (1977); Zhao et al. (2013)). Additionally, in the case of buoyant vortex rings in incompressible flows, it has been found that initially the cross section of the core decreases as the ring radius increases, which is as expected due to the conservation of the volume of the vorticity containing fluid (Bond and Johari (2010); Zhao et al. (2013)). This process makes the ring increasingly slender and continues until the core becomes unstable and turbulent. At this point, the thickness of the core starts to increase, and the ratio of the core radius to the ring radius remains approximately constant for a period of time. Eventually the vorticity from the core expands to most of the bubble and causes the destruction of the vortex ring structure as characterized in Figure 2. In the case of nonbuoyant rings, the instability also leads to an expansion of the core, although this process occurs more rapidly due to the lack of the stabilizing influence that spatial density variations can give (Maxworthy (1974)).

In all cases, the instability of the core is known to appear first in the form of stationary azimuthal waves (Maxworthy (1972); Dazin et al. (2006a)). The mechanism involved has been explained as inviscid and related to the straining field in the neighborhood of the core induced by the rest of the ring (Widnall and Sullivan (1973); Widnall et al. (1974); Widnall and Tsai (1977)), and more recently within the more general framework of elliptical instabilities (Kerswell (2002)). The growth of the azimuthal waves is observed to lead to the excitation of harmonics and subharmonics, which are accompanied by the development of an azimuthal flow, or solitary wave, which results in the loss of azimuthal symmetry (Maxworthy (1977); Nolan (2001); Naitoh et al. (2002)). After this transition, the ring with a turbulent core is seen to propagate for long distances without apparent changes in its characteristics, which suggests that some stabilizing mechanism is at play. Eventually nonlinear effects lead to a turbulent state that involves the whole ring. For nonbuoyant vortex rings, recent experimental and numerical results describe this stage in terms of the development of secondary vortical structures around the core that are periodically shed into a wake, resulting in the progressive decrease of the ring circulation and velocity of propagation, eventually leading to its disintegration (Weigand and Gharib (1994); Dazin et al. (2006a,b); Bergdorf et al. (2007); Archer et al. (2008); Gan and Nickels (2010); Gan et al. (2011)).

Overall, the experimental evidence for buoyant vortex ring is more limited and appears to indicate a more robust core, which persists for a longer time after the instability has initiated (Maxworthy (1977); Bond and Johari (2010); Zhao et al. (2013)). Even after the core becomes turbulent, the perturbations to its vorticity field are found to be mainly constrained to the azimuthal direction, whereas in the bubble the vorticity appears to have a more 3D character and smaller amplitude. Only in the later stages of the transition it is observed that the core radius becomes comparable to the ring radius, and the accompanying cancellation of vorticity leads to a collapse of the ring, described as “catastrophic” by Maxworthy (1977). This seems to indicate that toward the end of the transition process the evolution of buoyant vortex rings has parallels to those of nonbuoyant rings.

There is substantial scope to further study the evolution of buoyant vortex rings in stratified media by means of laboratory-scale experiments, numerical simulations, and by re-evaluating historic records of nuclear clouds (Slaughter (2015); Schmitt (2016)). Until that information becomes available, we use the existing data to develop our model of the nuclear cloud under the assumption that certain properties of vortex rings are generic and relevant to a wide range of configurations. Following previous observations, we propose to subdivide the evolution of the vortex ring in the cloud into three stages, which we denote the *laminar*, *similar*, and *turbulent* regimes. The laminar stage corresponds to the period from the vortex ring formation to the transition of the core to a turbulent state. In buoyant vortex rings, the conservation of the core volume and the increase in ring radius make the ratio between the two radii, $\tau = \epsilon / r_c$, vary with time.

Assuming the core to be a torus with initial volume V_0, r_c and ϵ are then related by

$$V_0 = 2\pi^2 r_c \epsilon^2. \tag{53}$$

This change in the vorticity distribution with time indicates that the similarity assumption on which (1) is based is not valid. In fact, under the assumption that the buoyant content and circulation of the core remain constant during the laminar regime, and taking the vorticity distribution to be uniform and confined to a thin core, relations (39), (41), and (53) can be combined to obtain an expression for the entrainment parameter,

$$\alpha = \frac{dr_c}{dz_c} = \frac{B_c}{\Gamma_c^2}\left(\frac{3}{2}\ln r_c + c\right)^{-1}, \tag{54}$$

where c is a constant given by

$$c = \ln 8\sqrt{\frac{2\pi}{V_0}} - \frac{1}{4}. \tag{55}$$

Equation (54) illustrates that in this nonsimilar regime, the entrainment parameter is not constant but decreases as the radius of the ring grows.

The analysis of Widnall et al. (Widnall and Sullivan (1973); Widnall et al. (1974); Widnall and Tsai (1977)) for nonbuoyant vortex rings has shown that the laminar core is always linearly unstable to normal modes in the form of stationary azimuthal waves. Using an asymptotic expansion for the flow around the core in terms of the ratio τ, they found that the wave number of the most unstable mode, κ, is of the order of the core radius, satisfying

$$\kappa\epsilon = \tilde{c}, \tag{56}$$

with $\tilde{c} \approx 2.5$. Since the number of waves around the circumference of the core, n, has to be an integer, it must satisfy

$$\kappa r_c = n, \tag{57}$$

and using (56) we obtain

$$\frac{\kappa\epsilon}{\tau} = \frac{\tilde{c}}{\tau} = n. \tag{58}$$

This shows that the instability will occur only for certain values of τ (actually for an interval around those values). Within the same analysis, it was found that the growth rate of the most unstable mode, Ω, follows

$$\Omega \sim \ln n. \tag{59}$$

From (58) and (59) we can deduce that during the laminar regime and as the radius of the ring increases and ϵ decreases with time, instability modes with different wave numbers and a larger n will be excited. If the rate of growth of the ring radius is fast enough, those unstable waves might not have enough time to grow to a sufficiently large amplitude to trigger nonlinear effects, before regressing into stable modes. As time progresses, (39) indicates that the rate of growth of the ring radius will decrease, while (59) shows that the growth rate of the unstable modes will increase. It can then be expected that as τ decreases, the transition to turbulence will become more likely. We propose then to characterize the initiation of the core

instability in terms of τ reaching a critical value. For nonbuoyant vortex rings, Maxworthy (1977) found that after the core becomes turbulent, the value of τ adopts an approximately constant value of 0.1, which remains for a substantial part of the following ring trajectory. We will assume that this observation applies to the case of buoyant vortex rings, and we identify τ reaching the value 0.1 with the transition from the laminar to the similar regime.[¶]

As the core evolves into a turbulent state, there is little understanding of the processes that convey to the ring its apparent robustness. The development of secondary vortical structures seems to play an important role in the later stage of the transition to turbulence, but their evolution is highly nonlinear and poorly understood. These structures appear to become increasingly complex in characteristics and size and are seen to be shed progressively into a wake (Archer et al. (2008)). During this stage, the circulation of the ring is found to decrease in discrete steps, resulting also in a reduction of its velocity of propagation (Weigand and Gharib (1994)). Eventually a transition is observed to a new regime where the circulation decreases more continuously and rapidly, approximately in a linear manner with time, and the distinction between the core and the bubble is lost (Weigand and Gharib (1994)).

The closer experimental configuration to the case of the nuclear cloud appears to be the study by Maxworthy (1977). In that case, an initially nonbuoyant vortex ring was allowed to evolve in a uniform medium until the development of the azimuthal instability. From that point onward, the ring entered a stratified medium with a density scale height that was large in comparison with the dimensions of the ring bubble. Maxworthy found the initial ring evolution to be similar to the nonbuoyant case, except for the vorticity generated at the interface between the bubble and the atmosphere (the vortex sheet in our model), which initially appears to have little interaction with the core. Following the similarity phase, he observed that the radius of the core increased to become commensurate to that of the bubble, which then led to a gradual loss of circulation and the deceleration of the ring in a similar manner as observed in nonbuoyant vortex rings.

These experimental results seem to indicate that during the similarity regime there is a competition between the radial growth of the ring, as determined by its buoyant content, and the turbulent diffusion of vorticity out of the core, with the former preventing the vorticity from reaching the axis of the ring. During the similarity regime, these two effects are approximately balanced to give a constant τ value. This mechanism is expected to become less effective as the rate of radial growth of the core decreases with time (c.f. 39). At the same time, the circulation of the bubble due to atmospheric stratification will in general increase in magnitude during the cloud evolution. In a stable atmosphere, it will have an opposite sign to the circulation in the core, and it will oppose its self-induced vertical motion. Thus we can expect the vorticity in the bubble to have a destabilizing effect on the ring evolution, especially when its magnitude becomes comparable to the core circulation.

We propose two criteria to determine the end of the similarity regime. One is based on the radial velocity of the core decreasing to a certain critical value, and the other on the amplitude of the circulation of the bubble becoming commensurate to that of the core. Our critical value for the former is determined on the few cases studies, as presented below. In those cases it was found that a change in the evolution of the radial cloud dimension appears to occur when the nondimensional radial velocity reached a value of around 0.04, which we adopted as marking the transition to the turbulent regime.[‖] In terms of the second criterion,

[¶]This is a simplification, since Maxworthy (1977) results appear to indicate that the core radius grows during the transition to the similarity regime, suggesting that τ is likely to reach values less than 0.1 during the laminar stage.

[‖]The temporal variation of the ring radius is a quantity amenable to measurements from historic records or laboratory experi-

we take the critical value of the bubble circulation to correspond to 50% of the core circulation, which quantifies the degree of coupling between the two vorticity regions. We assume that the end of the similarity regime is reached once either of the two criteria is met, the first to occur being determined by the initial characteristics of the ring and the stratification of the atmosphere.

The final or turbulent stage of the cloud evolution is characterized by the break down of the core as a distinct vortical structure, which leads to the shedding and cancellation of the core and bubble vorticity. The vortex ring is eventually replaced by series of smaller vortices that progressively resemble those typically found in atmospheric flows. At this point, the model proposed here will cease to be valid, and alternative physical and numerical implementation should be adopted (Arthur et al. (2021)). During this stage we consider the behavior of the cloud to be close to that of nonbuoyant vortex rings, and following the experimental results by Weigand and Gharib (1994), we propose a linear decrease of the circulation of the core and bubble with time, caused by vorticity cancellation and the shedding of small vortical structures into the wake. Additionally, it is likely that the break down of the core will promote the mixing with the ambient air and the cessation of a well-defined ring bubble. Consequently we assume the baroclinic source of vorticity as computed from (47) to become secondary at this stage, and we impose instead a decay of the bubble and core circulation of the form

$$\frac{d\,|\Gamma_c|}{dt} = k_c, \tag{60}$$

$$\frac{d\,|\Gamma_b|}{dt} = k_b, \tag{61}$$

where k_c and k_b are negative constants. In the work by Weigand and Gharib (1994), the value of the decay rate for the total circulation is of the order of -0.1 (in nondimensional units), and we adopted this value for both k_b and k_c in the examples below. Finally, the selection of a physical parameter or critical value as a means to identifying the end of the turbulent regime is less clear cut than for the other two cases. In the results presented below we adopted as criterion to end the computation that the circulation in the core had decayed to 10% of its initial value.

4.2 SCALING RELATIONS

The film records of nuclear tests (Spriggs and Gaunt (2011)) show that the fireball follows a trajectory similar to that observed in laboratory studies of buoyant bubbles in fluids (Walters and Davidson (1963), where a region of much lower density than the environment accelerates and "rolls-up" to form a vortex ring (Figure 3). In nuclear burst configurations where there is little interaction with reflected shock waves, it is natural to suggest that the same scaling relations will apply in both cases. In the simple configuration where the density perturbation is spherical and has uniform density, the characteristic length (L_0) of the system can be taken to be the radius of the sphere and the characteristic time can be defined by

$$T_0 = \sqrt{\frac{L_0\,\rho_a}{g\,(\rho_a - \rho_c)}}, \tag{62}$$

where ρ_c is the density of the perturbation and ρ_a is the ambient density. These quantities also provide scales for the velocities (L_0/T_0) and the circulations (L_0^2/T_0) and imply that the length and time scales of the system vary with the buoyant content of the bubble as $B_c^{1/3}$ and $B_c^{1/6}$, respectively, with B_c defined by (35).

ments and we expect that future studies will make it possible to determine this value with grater certainty.

In the case of the nuclear fireball, the complex density profile means that the boundary of the equivalent bubble is not unambiguously defined. Additionally, the interaction with other structures, which can affect the spherical symmetry and introduce additional sources of vorticity, makes it necessary to define effective values of the perturbation radius and density that can be used in combination with (62). Here we will follow a simplified description of the nuclear fireball and early cloud evolution to obtain an order of magnitude estimate to those effective quantities. Initially we will consider the conditions of an air nuclear burst, where the interaction with external structures is minimal and the fireball can be taken to be approximately spherical.

From the energy associated to the burst, around 70% initially takes the form of primary thermal radiation (mainly soft x-rays) that are absorbed within a few feet from the weapon location, forming an isothermal fireball. This energy is subsequently transformed into secondary thermal radiation and blast effects. Both processes drive the growth of the fireball, with the most external boundary initially being determined by the radiation front but later by the primary shock wave. Once pressure equilibrium has been achieved with the atmosphere, a region of low density and high temperature remains around the location of the burst. The complex characteristics of the resulting density profile reflect the multiplicity of processes by which the air is heated (Glasstone and Dolan (1977); Zeldovich and Raizer (2002)).

The physical mechanisms prevalent during the evolution of the fireball vary with time, and this results in different scaling relations. Once the shock front has emerged from the fireball and while the atmospheric pressure can be considered negligible compared to the blast overpressure, the only parameters defining the problem are the energy of the burst and the density of the unperturbed air. In this case, there are no characteristic time and length scales, making it possible the use of self-similar solutions (Taylor (1950a,b); Sedov (1993). Nevertheless, the evolution of the fireball into a vortex ring occurs over a period of seconds for a kiloton range yield, by which time the amplitude of the pressure perturbations will have become small in comparison to the atmospheric pressure (p_0). In this limit, the sphere associated to the adiabatic work equivalent to the energy release would have a radius of the order of

$$R_0^B \sim \left(\frac{Y}{p_0}\right)^{1/3}, \tag{63}$$

where Y is the yield of the weapon. Contained within this volume is the fireball determined by thermal radiation, whose radius can be approximated by (Glasstone and Dolan (1977)),

$$R_0^R = 67\, Y^{0.4}, \tag{64}$$

where the length is measured in meters and the yield in kilotons.

These relations indicate that, for example, for a yield of 1 Kt, the two radii will be $R_0^B \approx 370$ m and $R_0^R = 67$ m. At this stage we do not know what effective radius should be used to determine the scales of the problem, but we expect the value of L_0 to be in between R_0^B and R_0^R. The limited analysis of nuclear cloud measurements carried out so far appears to suggest a scaling of the form (63), and a good fit to the initial radii has been obtained with

$$L_0 = 120\, Y^{1/3}, \tag{65}$$

which is also in agreement with the radius of the density well obtained from radiation hydrodynamic calculations for a 1 Kt burst at sea level (without surface interactions) (Needham and Crepeau (1981)) and with the estimate by Taylor (1950b).

To determine an order of magnitude for the effective density differences to be used in (62), we consider an estimate to the upper bound of the temperature in the fireball. Although at early times the temperatures are of the order of hundred of thousands of degrees, adiabatic expansion and radiation losses result in substantial cooling in time scales much shorter than those associated to the formation of the vortex ring. The largest fraction of the losses by thermal radiation occurs in the form of a cooling wave (Zeldovich and Raizer (2002)), which reduces the temperature at the center of the fireball to about 10,000 K within a tenth of a second after the burst. In the following seconds, further cooling by radiation occurs at a much lower pace, and its importance is overtaken by hydrodynamic effects and the mixing with ambient air. Since the photographic evidence indicates that for the yields of interest the fireball is still luminous during the formation of the vortex ring, we estimate the effective temperature to be of the order of thousands degrees. In the example calculations included below, the effective density required to determine the length scale, which was also taken to be that of the core, was set at 10% of that of the atmosphere at the height of burst. Assuming an ideal gas approximation, this represents a temperature of the order of 4,000 K. The model also requires a value for the initial density of the bubble, which parameterizes the heating of the air around the effective fireball as well as the entrainment of cooler air and other materials during the formation of the vortex ring. In the case of an air burst, we take the density of the bubble to be 90% of that of the atmosphere at the height of burst.

The initial conditions of the model correspond to the buoyant vortex ring shortly after it was formed from the fireball. The radius of the ring and the length scale of the system are taken to be equal to the radius of the effective fireball, whose volume is assumed to be equal to the initial volume of the core (assumed to be a torus), so that the core radius satisfies $\epsilon \approx 0.46\, L_0$. In laboratory studies of vortex rings formed by the release of buoyant fluid it has been found that the nondimensional circulation has a value of approximately 5 (Lundgren et al. (1992)), which we also adopt here.

In the experimental study of vortex ring formation from bubbles in water, Walters and Davidson (1963) found that initially the bubbles were subject to an acceleration of twice that of gravity, before a marked change in behavior was observed, indicating the formation of the vortex ring. The duration of this initial phase was approximately one unit of nondimensional time, and the associated bubble displacement approximately one scaled length. Here we take the same values as the initial time and height of the ring for the calculation, where those quantities are measured from the time and height of the burst, respectively.

The characteristics of the cases where the interactions of the fireball with other structures become important are more involved and currently only partially understood. Initial results (Moresco et al. (2014)) show that a marked reduction in the ring circulation can occur as a result of the interaction between shock waves and the fireball, such as those caused by the reflection of the main blast wave from nearby boundaries. The physical processes responsible for this change are the deformation of the fireball (Shapiro and Kanak (2002); Bond and Johari (2005); Lai et al. (2015)) and the generation of vorticity by the pressure gradients at the shock front. Here we use a simplified parameter representation of these effects by multiplying the core circulation of the initial ring by a factor, which we estimated from the results in Moresco et al. (2014). We also expect the interaction with the ground for bursts at low altitude to result in enhanced mixing at the fireball surface and the entrainment of materials such as soil, which will affect the overall buoyant content of the ring. Until these processes are better understood, here we propose to parameterize these effects by a change in the initial density of the bubble, which we expect to gradually increase with the amount of mass of cooler material entrained as the height of burst is decreased.

Here we only consider simple configurations where the only structure the fireball can interact with is the

ground. In line with the scaling (65), we parameterize the interaction with the boundary in terms of a scaled height of burst, *SHOB*, defined by

$$SHOB = \frac{HOB}{Y^{1/3}}, \tag{66}$$

where *HOB* is the nominal height of burst (the vertical distance to the ground).

It has been common practice in the past to represent the effect of the boundary in bursts close to the ground by means of an effective yield, which for example in the case of a surface detonation is taken to be double the nominal yield (Glasstone and Dolan (1977)). This change is intended to capture the reflection of part of the released energy back to fireball, which would affect multiple physical processes, including the transport of radiation and the evolution of the blast wave. In turn, this will be manifested in the characteristics of the effective fireball, such as its shape, dimensions, and temperature profile, which as described above, will impact the properties of the vortex ring. By describing some of the properties of the ring as functions of the scaled height of burst, our model also captures this ground interaction, although through different physical variables. While attractive from a computational perspective, both approaches are oversimplifications of these complex interactions, and further research in this area is warranted.

4.3 EXAMPLES

We present below a comparison of the results obtained with the model described to cloud measurements recorded from three above ground nuclear tests carried out by the United States at the Nevada Test Site. These particular tests were chosen to exemplify the applicability of the model to different yields and height of bursts. The parameters used in these cases are listed in Table 1, where Γ^* refers to the factor multiplying the core circulation to reflect the interaction with the boundary, and $\Delta\rho_c$ refers to the initial relative difference of potential density of the bubble with respect to the atmosphere (in the notation used above this corresponds to $(\rho_b - \rho_a)/\rho_a$). The meteorological soundings were taken from historic records from the time of the tests (AWS (1993a,b)), and the weapon yield (which seems to be reported with an uncertainty of 0.1 Kt) as well as the cloud measurements were taken from Hawthorne (1979). The records of cloud dimensions were reported in the form of an interpolation of the original measurements, and it is not clear what the associated uncertainties are. There are also marked differences between the values obtained by different methods, for example from film analysis and theodolites measurements. Note that all the methodologies employed were based on visual determinations of cloud boundaries, which are subject to the visibility of material transported by the cloud and do not exactly reflect the underlying air flow. These differences are likely to be more pronounced at later times, when the cloud becomes progressively depleted of condensed mass. As a consequence, we expect the uncertainties in the comparison of the model results to these measurements to be large.

Table 1. Parameter values for the three nuclear tests studied.

Test	Yield[Kt]	*HOB*[m]	*SHOB*[m/kt$^{1/3}$]	Γ^*	$\Delta\rho_b$
Teapot Moth	2	91	73	0.97	0.9
Teapot Tesla	7	91	48	0.95	0.95
Buster-Jangle Sugar	1.2	1	1	0.85	1.1

In figures 9–11, we compare the recorded cloud top height and radius with the computed values, which were obtained by adding to the calculated core height and radius the bubble vertical and horizontal lengths,

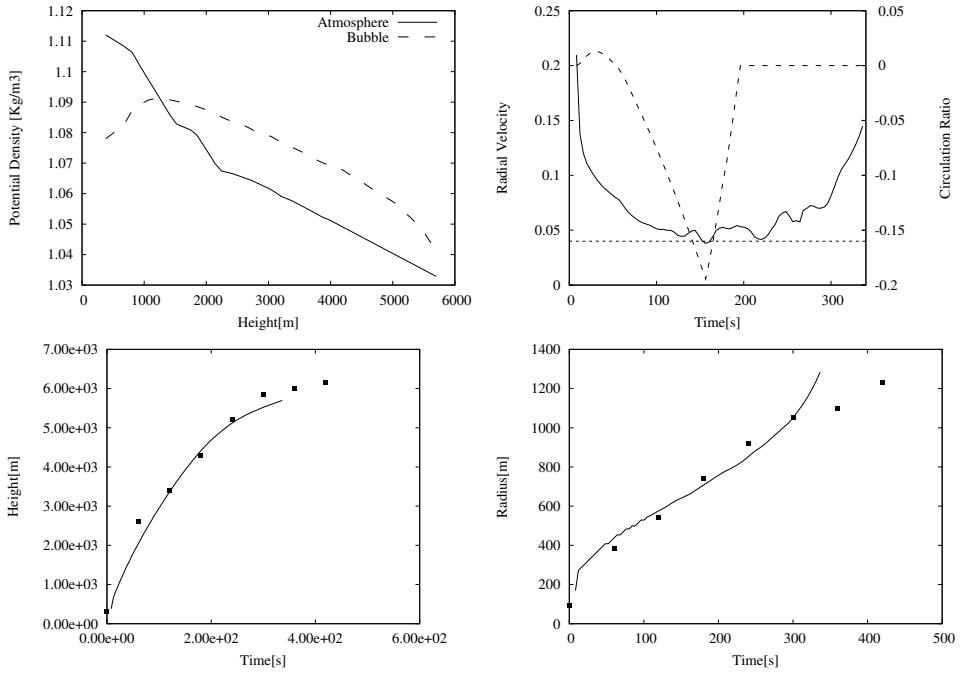

Figure 9. Comparison of model results and historic measurements for the Teapot Moth nuclear test. The plots correspond to interpolated atmospheric potential density (continuous line), bubble potential density (dashed line), radial core velocity (continuous line), ratio of bubble to core circulation (dashed line), computed cloud radius and top height (continuous lines), and cloud historic measurements (dots).

respectively. In the three cases, the computations compare favorably for the cloud heights, while the differences are larger for the cloud radii. This could be in part related to the irregularity of the bubble surface due to the baroclinic generation of vorticity and the associated instabilities. In both cases the discrepancies are more marked at later times, which is to be expected given the uncertainties in the description of the turbulent phase of the vortex ring, as already discussed.

Also shown are the evolution of the potential densities of the atmosphere and bubble. Except for the Sugar test, the bubble was initiated as lighter than the atmosphere, but because of entrainment and the stable stratification of the ambient air, this density difference quickly changed sign. This reversal of the density gradient is manifest in the change of sign of the source of vorticity on the bubble surface, which can also be seen in the plots of the ratio of bubble to core circulations. For the Moth and Tesla tests, there is an initial period in which this ratio is positive, indicating that the circulation of the bubble and the core had the same sign. In all three cases considered, the bubble density is higher for most of the cloud evolution, which results in an increasingly negative ratio of the circulations, a tendency that is more marked around strongly stable regions of the atmosphere, as can be seen by comparison with the plots of potential density versus height. After the transition to the turbulent regime the circulation ratio changes linearly with time, as the evolution of the circulations of the bubble and core are taken to be independent of the atmospheric stratification and to decrease at the same rate according to (60)–(61).

In Figures 9–11 we also show the variations of the radial velocity of the core (a moving mean) as a function

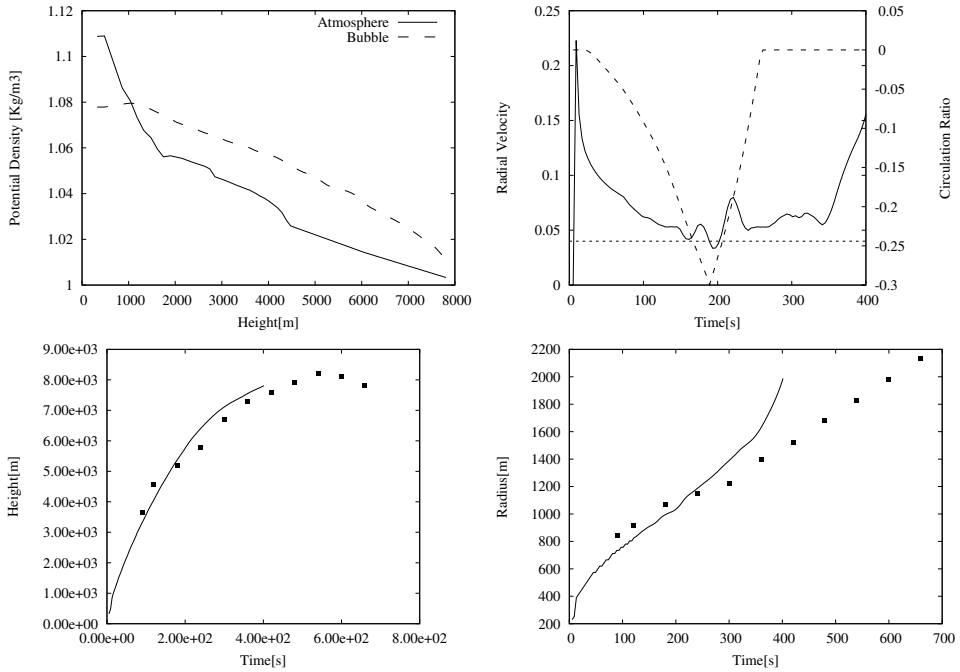

Figure 10. Comparison of model results and historic measurements for the Teapot Tesla nuclear test. The plots correspond to interpolated atmospheric potential density (continuous line), bubble potential density (dashed line), radial core velocity (continuous line), ratio of bubble to core circulation (dashed line), computed cloud radius and top height (continuous lines), and cloud historic measurements (dots).

of time, as well as the threshold value 0.04 used to identify the transition to the turbulent regime. In all cases the radial growth of the core appears to have slowed substantially before reaching this value, and the marked oscillations are an indication of the strong coupling between the vorticity in the core and the bubble. Comparing the plots of radial velocity and circulation ratio for the Moth and Tesla tests illustrates that the similarity regime in the model ended when the radial velocity crossed the imposed threshold, whereas for the Sugar test the trigger was the bubble circulation reaching 50% of the core circulation. Although future research is expected to provide refined criteria for the transition between the similarity and turbulent regimes, we believe that the observed behavior of the radial velocity is a robust indicator of conditions where instabilities are likely to develop.

As already explained, the scalings proposed here are just an order of magnitude approximation, and the associated errors are bound to be large. To exclude these uncertainties, in Figure 12 we plotted the calculated radius versus the height of the cloud. These results appear to indicate that the three-regime model of the cloud evolution is able to capture the measured changes in the cloud characteristics. The vertical lines in these plots indicate the heights the transitions between the regimes occurred (the line at the lowest height corresponding to the transition between the laminar and similar stages), and show that the similarity regime only applies to a fraction of the cloud trajectory. Nevertheless it still appears reasonable to propose a linear relation between the height and radius of the cloud, that is a constant value for the entrainment parameter, especially before the onset of the turbulent regime. This observation suggests that models based on the entrainment assumption (1) should provide reasonable results in many situations,

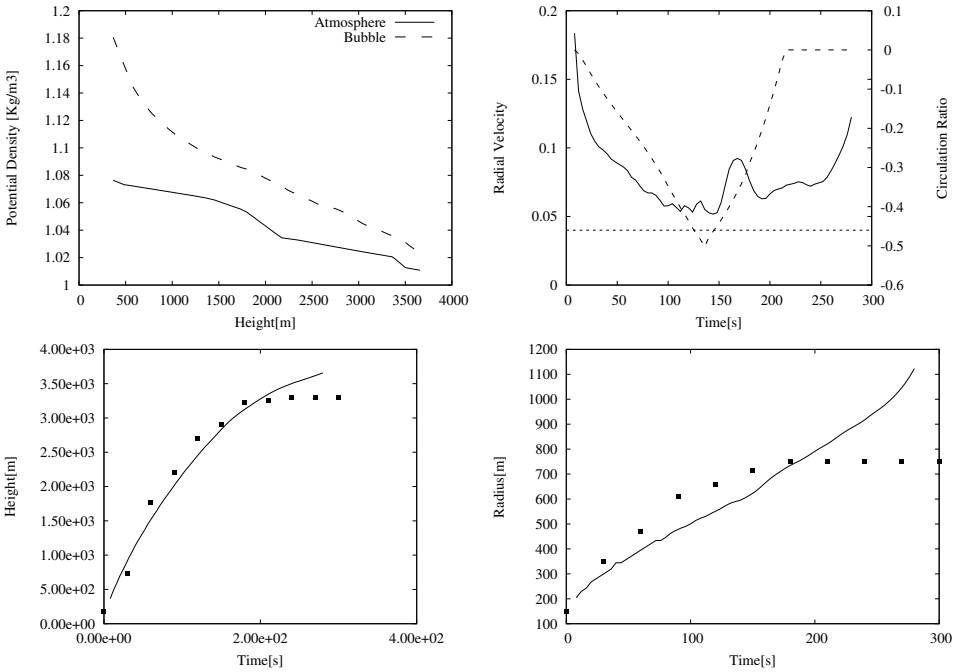

Figure 11. Comparison of model results and historic measurements for the Buster-Jungle Sugar nuclear test. The plots correspond to interpolated atmospheric potential density (continuous line), bubble potential density (dashed line), radial core velocity (continuous line), ratio of bubble to core circulation (dashed line), computed cloud radius and top height (continuous lines), and cloud historic measurements (dots).

which is supported by the extensive comparisons that have been done with nuclear test data (Francis et al. (2010)). In Figure 12 the dashed lines are approximation to this linear relation, whose slope (indicated) would correspond to the entrainment parameter α in (1). Our results also suggest that developing a parameterization of the entrainment parameter that is a function of the scaled height of burst and takes into account the variations caused by the vortex ring instabilities and changes in the atmospheric conditions, would be a valuable addition to cloud models based on the entrainment assumption, without substantially increasing their computational complexity.

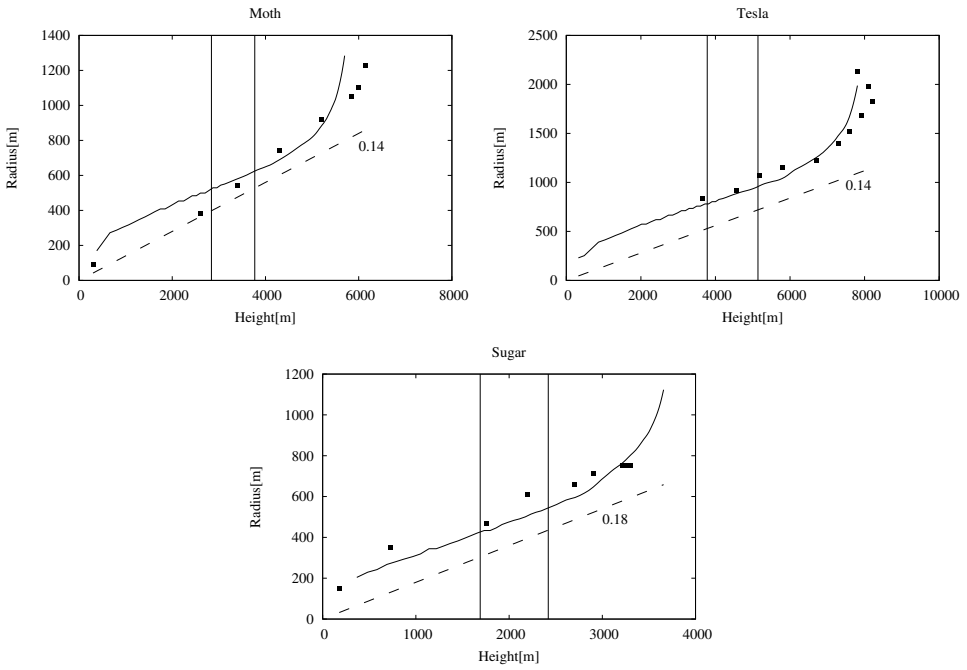

Figure 12. Comparison of model results with historic measurements for the three nuclear tests considered. Indicated are the heights at which transitions occurred between the stages of the cloud evolution and the entrainment parameters obtained from linear interpolations to the curves.

5. CONCLUSIONS

The purpose of this work was to develop a model of the nuclear cloud that provides better physical accuracy than the descriptions currently employed in operational settings, while maintaining the requirement of modest computational cost. The approach we followed is based on the properties of buoyant vortex rings, which are usually the dominant feature of nuclear clouds during most of their evolution. Although vortex ring models of the cloud have been proposed before (Huebsch (1966)), only in recent years have they become a viable option in operational settings as a result of a better understanding of these type of flows, as well as advances in numerical schemes and computational hardware.

One of the main advantages of this approach over traditional models based on Taylor's entrainment assumption (1) is that it provides a better characterization of the velocity field in the proximity of the cloud, which is crucial in describing the transport of condensed matter during cloud rise and the spatial distribution of radioactive weapon debris. Additionally, there is no requirement to specify an entrainment parameter as an input, as the radial expansion of the ring is solved explicitly. This is expected to give a description of the main cloud characteristics, such as stabilization height, that is more robust and responsive to changes in weapon emplacement and atmospheric conditions.

Our main assumption has been that the large-scale flow motions are determined by the vorticity attached to the ring. To reduce computational costs, we took advantage of the spatial concentration of the vorticity and decomposed it into two components: the core and a vortex sheet around the bubble. A discretization of the vorticity field into vortex elements resulted in a Lagrangian formalism to describe its evolution, with the benefit of being mesh-free and requiring only the solution of a set of ordinary differential equations. As an indication of the computational cost of the model, the calculations of the cloud evolution presented in Section 2 took about 5 minutes using a state-of-the-art desktop computer. Under the approximations discussed in Section 2, at any point in the domain the velocity field due to the ring can be obtained from the instantaneous vorticity distribution. When this is combined with an atmospheric wind velocity field, it is possible to describe the transport of particles or scalar fields by the cloud following a Lagrangian or Eulerian description. Examples of this type of calculations are shown in Figures 13 and 14.

Being a reduced model of the cloud, the proposed description is not free of parameters that need to be prescribed. As discussed in Section 4, those quantities can be related to physical properties of buoyant vortex rings, and in most cases it should be possible to determine their functional dependences from measurements obtained from historic nuclear cloud records or from laboratory experiments. The relatively good agreement that was obtained in the examples presented by using rough estimates of those quantities is an indication that there is margin to improve this description by including more data in the analysis. Certain requirements imposed on the model, such as the constancy of the buoyant content of the core, could be relaxed without incurring substantial additional computational costs, but these requirements were kept here because they are believed to be of the same order as the other approximations. In general, while designing the model we gave precedence to simplicity over accuracy until more data become available and better estimates of the errors incurred can be made.

One of the main shortcomings of the proposed model is the assumption of axisymmetry of the vortex ring. Although this is likely to be valid at early time, both the development of the instability of the core and the interaction with atmospheric flows (especially wind shear) are bound to break this symmetry (Lifschitz et al. (1996)). We consider the description presented here to capture the properties of the vortex ring on average and to be preferable to the substantial extra numerical cost that would involve abandoning this

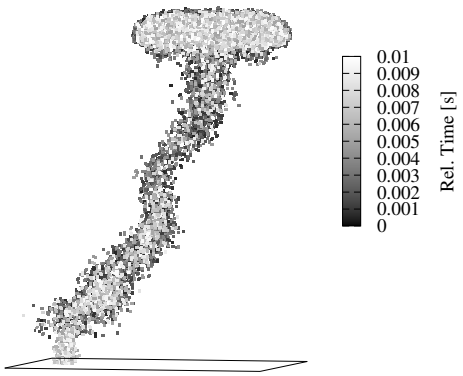

Figure 13. Example of the use of the vorticity model of the nuclear cloud to compute the transport of Lagrangian particles. The plot corresponds to the Tesla test at 4 minutes after the burst. Particle trajectories were computed using a Langevin equation approach (Durbin (1980)), and the gray scale indicates the Stokes relaxation time of the particles. Note, no effort was taken to distinguish between exposed and obscured particles for the given perspective.

assumption (Knio and Ghoniem (1990); Lindsay and Krasny (2001)). We still believe that further studying the impact of this approximation is warranted. In the same line, the assumption that the cross section of the core remains circular at all times is likely to be a source of error, especially when the interaction with the vorticity in the bubble becomes important. Representing the core of the ring with multiple vortex filaments (Brecht and Ferrante (1989)) would allow for a more accurate description of the vorticity field and is an approach that should be considered as computational power continues to evolve.

The characteristics of the vortex ring used as the initial condition in the model need to encapsulate the evolution of the fireball during the first few seconds after the burst. Multiple physical processes have to be considered to relate the properties of the ring, such as its radius, circulation, and buoyant content, to the characteristics of the weapon emplacement. This regime is still not well understood, but progress can be expected in the near future thanks to the advancement in first principles, high fidelity computational descriptions of the fireball (Duncan and Key (2019)), and ongoing efforts to reanalyze and expand the set of measurements from historic cloud records.

Experimental observations show that during most of the evolution of buoyant vortex rings, the core is turbulent, and a better understanding of the stability properties of these flows is likely to have a big impact on the accuracy of the computed cloud characteristics. Most of the results used in the development of the model were obtained for nonbuoyant vortex rings, and the analysis would benefit from further experimental and analytical studies. This lack of data has a bigger impact in the later stages of the cloud evolution, where we expect the uncertainty in the predictions from the model to grow accordingly. In particular, our treatment of the final or turbulent stage of the vortex ring is admittedly very simplistic. A smooth transition to the type of descriptions used for the dynamics of the atmosphere would be desirable but is still lacking. We can imagine that a formulation of atmospheric flows based on the vorticity field, perhaps within the

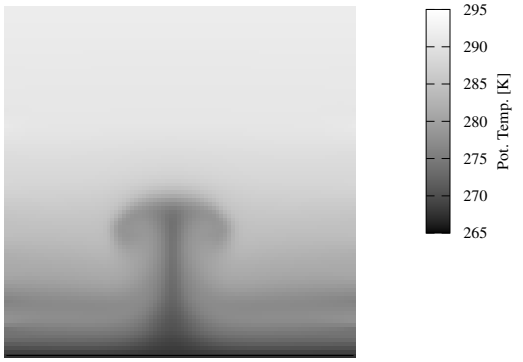

Figure 14. Example of the use of the vorticity model of the nuclear cloud to compute the transport of potential temperature in an Eulerian framework. The plot correspond to the Tesla test at 23 seconds after the burst. The computations were carried out using an upwind finite volume Eulerian scheme (Leveque (2002)) where the fluxes were calculated using the velocity determined by the vorticity field.

framework of the Large Eddy Simulation scheme (Mansfield et al. (1998)) could offer a natural bridge to the approach followed in this model.

It is our expectation that this work will fill a gap in the tool box of descriptions of the nuclear cloud, making it possible to obtain some characteristics of the solution that were previously only available from calculations on high-end computer platforms. Having the possibility to run this model side-by-side with current operational descriptions should benefit activities such as sample collection for forensic analysis, where planning is done within multiple time frames as input data become available. In the longer term, we believe this effort will support the development of a hierarchy of models with different levels of approximation and computational requirements. Having a good understanding of the physical approximations involved at each level of description will make it possible to determine their domain of applicability as well as quantify the associated errors and uncertainties. This in turn will allow users to make informed decisions on the best approach to employ for a given physical configuration and set of time constraints.

6. REFERENCES

Acton, E. (1980). A modelling of large eddies in an axisymmetric jet. *J. Fluid Mech.*, 98:1–31.

Advaith, S., Manu, K. V., Tinaikar, A., Chetia, U. K., and Basu, S. (2017). Interaction of vortex ring with a stratified finite thickness interface. *Phys. Fluids*, 29:093602.

Archer, P. J., Thomas, T. G., and Coleman, G. N. (2008). Direct numerical simulation of vortex ring evolution from the laminar to the early turbulent regime. *J. Fluid Mech.*, 598:201–226.

Arthur, R. S., Lundquist, K. A., Mirocha, J. D., Neuscamman, S., Kanarska, Y., and Nasstrom, J. S. (2021). Simulating nuclear cloud rise within a realistic atmosphere using the Weather Research and Forecasting model. *Atmos. Environ.*, 254:118363.

Ashurst, W. T. (1988). Numerical simulation of turbulent mixing layers via vortex dynamics. Report SAND77-8613, Sandia Laboratories.

AWS (1993a). Microfilm (1 reel) of upper air data for Yucca Flats Test Site, NV for February 18, 1955 through May 15, 1955. Report OL-A, USAFETAC/GCOO. M, Environmental Technical Applications Center.

AWS (1993b). Microfilm (1 reel) of upper air data for Yucca Flats Test Site, NV for October through December 1951. Report OL-A, USAFETAC/GCOO. M, Environmental Technical Applications Center.

Baden, S. B. and Puckett, E. G. (1990). A fast vortex method for computing 2D viscous flow. *J. Comput. Phys.*, 91:278–297.

Baird, J. P. (1987). Supersonic vortex rings. *Proc. Roy. Soc. A*, 409:59–65.

Baker, G. R., Meiron, D. I., and Orszag, S. A. (1982). Generalized vortex methods for free-surface flow problems. *J. Fluid Mech.*, 123:477–501.

Baker, G. R. and Shelley, M. J. (1990). On the connection between thin vortex layers and vortex sheets. *J. Fluid Mech.*, 215:161–194.

Batchelor, G. K. (1950). The application of the similarity theory of turbulence to atmospheric diffusion. *Quart. J. R. Met. Soc.*, 76:133–146.

Batchelor, G. K. (1953). The conditions for dynamical similarity of motions of a frictionless perfect-gas atmosphere. *Quart. J. R. Met. Soc.*, 79:224–235.

Batchelor, G. K. (1967). *An introduction to fluid dynamics*. Cambridge University Press.

Be Hagh, A. R. V., Carriveau, R., and Ting, D. S.-K. (2015). A balloon bursting underwater. *J. Fluid Mech.*, 769:522–540.

Beale, J. T. and Majda, A. (1982a). Vortex methods, I: Convergence in three dimensions. *Math. Comp.*, 39:1–27.

Beale, J. T. and Majda, A. (1982b). Vortex methods, II: Higher order accuracy in two and three dimensions. *Math. Comp.*, 39:29–52.

Bergdorf, M., Koumoutsakos, P., and Leonard, A. (2007). Direct numerical simulations of vortex rings at $\mathrm{Re}_\Gamma = 7500$. *J. Fluid Mech.*, 581:495–505.

Bond, D. and Johari, H. (2005). Effects of initial geometry on the development of thermals. *Exp. Fluids*, 39:589–599.

Bond, D. and Johari, H. (2010). Impact of buoyancy in vortex ring development. *Exp. Fluids*, 48:737–745.

Brecht, S. H. and Ferrante, J. R. (1989). Vortex-in-cell simulations of buoyant bubbles in three dimensions. *Phys. Fluids*, A 1:1166–1191.

Brecht, S. H. and Ferrante, J. R. (1990). Vortex-in-cell calculations in three dimensions. *Comput. Phys. Commun.*, 58:25–54.

Caflisch, R. E. and Li, X.-F. (1992). Lagrangian theory for 3D vortex sheets with axial or helical symmetry. *Trans. Theory Stat. Phys.*, 21:559–578.

Chang, C. and Llewellyn Smith, S. G. (2020). Axisymmetric contour dynamics for buoyant vortex rings. *J. Fluid Mech.*, 887:A28.

Chorin, A. J. (1973). Numerical study of slightly viscous flow. *J. Fluid Mech.*, 57:785–796.

Chorin, A. J. and Bernard, P. S. (1973). Discretization of a vortex sheet, with an example of roll-up. *J. Comput. Phys.*, 13:423–429.

Cody, W. J. (1965). Chebyshev polynomial expansions of complete elliptic integrals. *Math. Comp.*, 19:249–259.

Cotett, G.-H., Koumoutsakos, P., and Salihi, M. L. O. (2000). Vortex methods with spatially varying cores. *J. Comput. Phys.*, 162:164–185.

Crow, S. C. (1970). Stability theory for a pair of trailing vortices. *AIAA J.*, 8:2172–2179.

Dazin, A., Dupont, P., and Stanislas, M. (2006a). Experimental characterization of the instability of the vortex ring. Part I: Linear phase. *Exp. Fluids*, 40:383–399.

Dazin, A., Dupont, P., and Stanislas, M. (2006b). Experimental characterization of the instability of the vortex rings. Part II: Non-linear phase. *Exp. Fluids*, 41:401–413.

DeVoria, A. C. and Mohseni, K. (2018). Vortex sheet roll-up revisited. *J. Fluid Mech.*, 855:299–321.

Didden, N. (1979). On the formation of vortex rings: rolling-up and production of circulation. *J. Appl. Math. Phys. (ZAMP)*, 30:101–116.

Duncan, G. C. and Key, C. T. (2019). Progress towards a new CTH code verification & validation test suite. Report SAND2019-12020, Sandia Laboratories.

Durbin, P. A. (1980). A random flight model of inhomogenous turbulent dispersion. *Phys. Fluids*, 23:2151–2153.

Dutton, J. A. and Fichtl, G. H. (1969). Approximate equations of motion for gases and liquids. *J. Atmos. Sci.*, 26:241–254.

Dziedzic, M. and Leutheusser, H. J. (1996). An experimental study of viscous vortex rings. *Exp. Fluids*, 21:315–324.

Eldredge, J. D., Colonius, T., and Leonard, A. (2002). A vortex particle method for two-dimensional compressible flow. *J. Comput. Phys.*, 179:371–399.

Fink, P. T. and Soh, W. K. (1978). A new approach to roll-up calculations of vortex sheets. *Proc. Roy. Soc. A*, 362:195–209.

Foster, P. M. (1982). Particle fallout during plume rise. *Atmos. Environ.*, 16:2777–2784.

Fraenkel, L. E. (1970). On steady vortex rings of small cross-section in an ideal fluid. *Proc. Roy. Soc. A*, 316:29–62.

Fraenkel, L. E. (1972). Examples of steady vortex rings of small cross-section in an ideal fluid. *J. Fluid Mech.*, 51:119–135.

Francis, M. W., Jodoin, V. J., and Lefebvre, J. P. (2010). Study on the ability to predict yield from the stabilized height of a nuclear cloud. Report ORNL/TM-2010/209, Oak Ridge National Laboratory.

Fukumoto, Y. and Moffatt, H. K. (2008). Kinematic variational principle for motion of vortex rings. *Physica D*, 237:2210–2217.

Gan, L., Dawson, J. R., and Nickels, T. B. (2012). On the drag of turbulent vortex rings. *J. Fluid Mech.*, 709:85–105.

Gan, L. and Nickels, T. B. (2010). An experimental study of turbulent vortex rings during their early development. *J. Fluid Mech.*, 649:467–496.

Gan, L., Nickels, T. B., and Dawson, J. R. (2011). An experimental study of a turbulent vortex ring: a three-dimensional representation. *Exp. Fluids*, 51:1493–1507.

Garten, J. F., Arendt, S., Fritts, D. C., and Werne, J. (1998). Dynamics of counter-rotating vortex pairs in stratified and sheared environments. *J. Fluid Mech.*, 361:189–236.

Glasstone, S. and Dolan, P. J. (1977). *The fffects of nuclear weapons*. US Department of Defense.

Glezer, A. and Coles, D. (1990). An experimental study of a turbulent vortex ring. *J. Fluid Mech.*, 211:243–283.

Grabowski, D. W. and Telste, J. G. (1978). A discrete vortex simulation of a two-dimensional shear layer with prediction of hydrodynamic noise. Report DTNSRDC-78/050, David W. Taylor Naval Ship Research and Development Center.

Gray, D. D. and Giorgini, A. (1976). The validity of the Boussinesq approximation for liquids and gases. *Int. J. Heat Mass Transfer*, 19:545–551.

Hald, O. (1979). Convergence of vortex methods for Euler's equations. II. *SIAM J. Numer. Anal.*, 16:726–755.

Hald, O. and Prete, V. M. D. (1978). Convergence of vortex methods for Euler's equations. *Math. Comput.*, 32:791–809.

Hawthorne, H. A. (1979). Compilation of local fallout data from test detonations 1945–1962 extracted from DASA 1251. Volume I –Continental U.S. Tests. Report DNA 1251-1-EX, Defense Nuclear Agency.

Hicks, W. M. (1884). On the steady motion and small vibrations of a hollow vortex. *Phil. Trans. R. Soc. Lond. A*, 175:161–195.

Hill, F. M. (1975). A numerical study of the descent of a vortex pair in a stably stratified atmosphere. *J. Fluid Mech.*, 71:1–13.

Hill, M. J. M. (1894). On a spherical vortex. *Phil. Trans. R. Soc. Lond. A*, 185:213–245.

Huebsch, I. O. (1966). Turbulence, toroidal circulation and dispersion of fallout particles from the rising nuclear cloud. Report USNRDL-TR-1054, U. S. Naval Radiological Defense Laboratory.

Johari, H. (1992). Mixing in thermals with and without buoyancy reversal. *J. Atmos. Sci.*, 49:1412–1426.

Kanarska, Y., Lomov, I., Glenn, L., and Antoun, T. (2009). Numerical simulation of cloud rise phenomena associated with nuclear bursts. *Ann. Nucl. Energy*, 36:1475–1483.

Kaneda, Y. (1990). A representation of the motion of a vortex sheet in a three-dimensional flow. *Phys. Fluids A*, 2:458–461.

Kerswell, R. R. (2002). Elliptical instability. *Annu. Rev. Fluid Mech.*, 34:83–113.

Knio, O. M. and Ghoniem, A. F. (1990). Numerical study of a three-dimensional vortex method. *J. Comput. Phys.*, 86:75–106.

Krasny, R. (1986a). Desingularization of periodic vortex sheet roll-up. *J. Comput. Phys.*, 65:292–313.

Krasny, R. (1986b). A study of singularity formation in a vortex sheet by the point-vortex approximation. *J. Fluid Mech.*, 167:65–93.

Krasny, R. (1987). Computation of vortex sheet roll-up in the Trefftz plane. *J. Fluid Mech.*, 184:123–155.

Krasny, R. (1991). Vortex sheet computations: Roll-up, wakes, separation. *Lectures in Applied Mathematics*, 28:385–402.

Kuran, P. (2006). *How to photograph an atomic bomb*. VCE.

Lai, A. C. H., Zhao, B., Law, A. W. K., and Adams, E. E. (2015). A numerical and analytical study of the effect of aspect ratio on the behavior of a round thermal. *Environ. Fluid Mech.*, 15:85–108.

Lamb, H. (1932). *Hydrodynamics*. Cambridge University Press.

Lecoanet, D. and Jeevanjee, N. (2019). Entrainment in resolved, dry thermals. *J. Atmos. Sci.*, 76:3785–3801.

Leonard, A. (1980). Vortex methods for flow simulation. *J. Comput. Phys.*, 37:289–335.

Leveque, R. J. (2002). *Finite volume methods for hyperbolic problems*. Cambridge University Press.

Levine, J. (1959). Spherical vortex theory of bubble-like motion in cumulus clouds. *J. Meteor.*, 16:653–662.

Liepmann, H. W. and Roshko, A. (1985). *Elements of gasdynamics*. Dover Publications.

Lifschitz, A., Suters, W. H., and Beale, J. T. (1996). The onset of instability in exact vortex rings with swirl. *J. Comput. Phys.*, 129:8–29.

Lindsay, K. and Krasny, R. (2001). A particle method and adaptive treecode for vortex sheet motion in three-dimensional flow. *J. Comput. Phys.*, 172:879–907.

Lipps, F. B. and Hemler, R. S. (1982). A scale analysis of deep moist convection and some related numerical calculations. *J. Atmos. Sci.*, 39:2192–2210.

Lundgren, T. S. and Mansour, N. N. (1991). Vortex ring bubbles. *J. Fluid Mech.*, 224:177–196.

Lundgren, T. S., Yao, J., and Mansour, N. N. (1992). Microburst modelling and scaling. *J. Fluid Mech.*, 239:461–488.

Machta, L. (1950). Entrainment and the maximum height of an atomic cloud. *Bull. Am. Meteorol. Soc.*, 31:215–216.

Mahrt, L. (1986). On the shallow motion approximations. *J. Atmos. Sci.*, 43:1036–1044.

Mansfield, J. R., Knio, O. M., and Meneveau, C. (1998). A dynamics LES scheme for the vorticity transport equation: formulation and *a priori* tests. *J. Comput. Phys.*, 145:693–730.

Mao, X. and Hussain, F. (2017). Optimal transient growth on a vortex ring and its transition via cascade of ringlets. *J. Fluid Mech.*, 832:269–286.

Maxworthy, T. (1972). The structure and stability of vortex rings. *J. Fluid Mech.*, 51:15–32.

Maxworthy, T. (1974). Turbulent vortex rings. *J. Fluid Mech.*, 64:227–239.

Maxworthy, T. (1977). Some experimental studies of vortex rings. *J. Fluid Mech.*, 81:465–495.

McKim, B., Jeevanjee, N., and Lecoanet, D. (2020). Buoyancy-driven entrainment in dry thermals. *Q. J. R. Meteorol. Soc.*, 146:415–425.

Meiron, D. I., Baker, G. R., and Orszag, S. A. (1982). Analytic structure of vortex sheet dynamics. Part 1. Kelvin–Helmholtz instability. *J. Fluid Mech.*, 114:283–298.

Meleshko, V. V., Gourjii, A. A., and Krasnopolskaya, T. S. (2012). Vortex rings: history and state of the art. *J. Appl. Math. Sci.*, 187:772–808.

Meng, J. C. S. (1978). The physics of vortex-ring evolution in a stratified and shearing environment. *J. Fluid Mech.*, 84:455–469.

Meng, J. C. S. and Thomson, J. A. L. (1978). Numerical studies of some nonlinear hydrodynamic problems by discrete vortex element methods. *J. Fluid Mech.*, 84:433–453.

Milne-Thomson, L. M. (2011). *Theoretical hydrodynamics*. Dover Publications.

Moffat, H. K. and Moore, D. W. (1978). The response of Hill's spherical vortex to a small axisymmetric disturbance. *J. Fluid Mech.*, 87:749–760.

Moore, D. W. (1971). Finite amplitude waves on aircraft trailing vortices. Technical AFOSR-1804-69, Air Force Office of Scientific Research.

Moore, D. W. (1979). The spontaneous appearance of a singularity in the shape of an evolving vortex sheet. *Proc. Roy. Soc. A*, 365:105–119.

Moore, D. W. (1985). The effect of compressibility on the speed of propagation of a vortex ring. *Proc. Roy. Soc. A*, 397:87–97.

Moresco, P., Harris, T. E., and Jodoin, V. (2014). Vorticity generation by the instantaneous release of energy near a reflective boundary. *Phys. Rev. E*, 90:023002.

Morrison, H. and Peters, J. M. (2018). Theoretical expressions for the ascent rate of moist deep convective thermals. *J. Atmos. Sci.*, 75:1699–1719.

Morton, B. R., Taylor, G., and Turner, J. S. (1956). Turbulent gravitational convection from maintained and instantaneous sources. *Proc. Roy. Soc. A*, 234:1–23.

Munz, C.-D., Roller, S., Klein, R., and Geratz, K. J. (2020). The extension of incompressible flow solvers to the weakly compressible regime. *Comput. Fluids*, 210:104651.

Naitoh, T., Fukuda, N., Gotoh, T., Yamada, H., and Nakajima, K. (2002). Experimental study of axial flow in a vortex ring. *Phys. Fluids*, 14:143–149.

Needham, C. E. and Crepeau, J. E. (1981). The DNA nuclear blast standard (1 Kt). Report DNA 5648T, Defense Nuclear Agency.

Nitsche, M. (2001). Self-similar shedding of vortex rings. *J. Fluid Mech.*, 435:397–407.

Nitsche, M. and Krasny, R. (1994). A numerical study of vortex ring formation at the edge of a circular tube. *J. Fluid Mech.*, 276:139–161.

Nitsche, M. and Strickland, J. H. (2002). Extension of the gridless vortex method into the compressible flow regime. *J. Turbulence*, 3:1–6.

Nolan, D. S. (2001). The stabilizing effects of axial stretching on turbulent vortex dynamics. *Phys. Fluids*, 13:1724–1738.

Norbury, J. (1973). A family of steady vortex rings. *J. Fluid Mech.*, 57:417–431.

Norment, H. G. (1979). DELFIC. Department of Defense fallout prediction system. Volume I — Fundamentals. Report DNA 5159F-1, Defense Nuclear Agency.

Ogura, Y. and Phillips, N. A. (1962). Scale analysis of deep and shallow convection in the atmosphere. *J. Atmos. Sci.*, 19:173–179.

Orlandi, P. and Carnevale, G. F. (2020). Numerical simulations of thermals with and without stratification. *J. Fluid Mech.*, 899:A37.

Pergaud, J., Masson, V., Malardel, S., and Couvreaux, F. (2009). A parameterization of dry thermals and shallow cumuli for mesocale numerical weather prediction. *Boundary-Layer Meteorol.*, 132:83–106.

Pope, S. B. (2000). *Turbulent Flows*. Cambridge University Press.

Pozrikidis, C. (1986). The nonlinear instability of Hill's vortex. *J. Fluid Mech.*, 168:337–367.

Pozrikidis, C. (2000). Theoretical and computational aspects of the self-induced motion of three-dimensional vortex sheets. *J. Fluid Mech.*, 425:335–366.

Prandtl, L. and Tietjens, O. G. (1934). *Fundamentals of hydro- and aeromechanics*. Dover Publications.

Richards, J. M. (1961). Experiments on the penetration of an interface by buoyant thermals. *J. Fluid Mech.*, 11:369–384.

Rosenhead, L. (1931). The formation of vortices from a surface of discontinuity. *Proc. Roy. Soc. A*, 134:170–192.

Saffman, P. G. (1970). The velocity of viscous vortex rings. *Studies App. Math.*, 49:371–380.

Saffman, P. G. (1992). *Vortex dynamics*. Cambridge University Press.

Saffman, P. G. and Baker, G. R. (1979). Vortex interactions. *Annu. Rev. Fluid Mech.*, 11:95–122.

Sanchez, O., Raymond, D. J., Libersky, L., and Petschek, A. G. (1989). The development of thermals from rest. *J. Atmos. Sci.*, 46:2280–2292.

Saunders, P. M. (1962). Penetrative convection in stably stratified fluids. *Tellus*, 14:177–194.

Schmidt, W. (1941). Turbulente ausbreitung eines stromes erhitzter luft. *Z. Angew. Math. Mech.*, 21:265–278.

Schmitt, D. T. (2016). *Position and volume estimation of atmospheric nuclear detonations from video reconstruction*. PhD thesis, Air Force Institute of Technology.

Scorer, R. S. (1957). Experiments on convection of isolated masses of buoyant fluid. *J. Fluid Mech.*, 2:583–594.

Scorer, R. S. and Davenport, L. J. (1970). Contrails and aircraft downwash. *J. Fluid Mech.*, 43:451–464.

Sedov, L. I. (1993). *Similarity and dimensional methods in mechanics*. CRC Press.

Shapiro, A. and Kanak, K. M. (2002). Vortex formation in ellipsoidal thermal bubbles. *J. Atmos. Sci.*, 59:2253–2269.

Shariff, K. and Leonard, A. (1992). Vortex rings. *Annu. Rev. Fluid Mech.*, 24:235–279.

Shaw, S. and McHugh, J. P. (2019). Evolution of a line vortex in stratified flow. *Phys. Rev. Fluids*, 4:064803.

Shirgaonkar, A. A. and Lele, S. K. (2006). On the extension of the Boussinesq approximation for intertia dominated flows. *Phys. Fluids*, 18:066601.

Slaughter, R. C. (2015). *Multidimensional analysis of atmospheric nuclear detonations*. PhD thesis, Air Force Institute of Technology.

Sod, G. A. (1991). A compressible vortex method with application to the interaction of an oblique shock wave with a boundary layer. *Appl. Numer. Math.*, 8:257–273.

Sohn, S.-I. (2004). Vortex model and simulations for Rayleigh–Taylor and Richtmayer–Meshkov instabilities. *Phys. Rev. E*, 69:036703.

Spalart, P. R. (1996). On the motion of laminar wing wakes in a stratified fluid. *J. Fluid Mech.*, 327:139–160.

Spiegel, E. A. and Veronis, G. (1959). On the Boussinesq approximation for a compressible fluid. *Asprophys. J.*, 131:442–447.

Spriggs, G. D. and Gaunt, R. (2011). Scientific objectives of scanning project. Report LLNL-PRES-491856, Lawrence Livermore National Laboratory.

Sullivan, J. P., Widnall, S. E., and Ezekiel, S. (1973). Study of vortex rings using laser doppler velocimeter. *AIAA J.*, 11:1384–1389.

Sutton, O. G. (1947). The atom bomb trial as an experiment in convection. *Weather*, 2:105–110.

Sutton, O. G. (1950). Note on "Entrainment and the maximum height of an atomic cloud" by Lester Machta. *Bull. Am. Meteorol. Soc.*, 31:217–218.

Taylor, G. (1950a). The formation of a blast wave by a very intense explosion. I. Theoretical discussion. *Proc. Roy. Soc. A*, 201:159–174.

Taylor, G. (1950b). The formation of a blast wave by a very intense explosion. II. The atomic explosion of 1945. *Proc. Roy. Soc. A*, 201:175–186.

Taylor, G. I. (1945). Dynamics of a mass of hot gas rising in air. Report MDDC 919, U. S. Atomic Energy Commission.

Thompson, R. S., Snyder, W. H., and Weil, J. C. (2000). Laboratory simulation of the rise of buoyant thermals created by open detonation. *J. Fluid Mech.*, 417:127–156.

Thornber, B., Mosedale, A., Drikakis, D., Youngs, D., and Willians, R. J. R. (2008). An improved reconstruction method for compressible flows with low Mach number features. *J. Comput. Phys.*, 227:4873–4894.

Tryggvason, G. (1989). Simulation of vortex sheet roll-up by vortex methods. *J. Comput. Phys.*, 80:1–16.

Tryggvason, G., Dahm, W. J. A., and Sbeih, K. (1991). Fine structure of vortex sheet rollup by viscous and inviscid simulation. *Trans. ASME, J. Fluids. Eng.*, 113:31–36.

Tung, C. and Ting, L. (1967). Motion and decay of a vortex ring. *Phys. Fluids*, 10:901–910.

Turner, J. S. (1957). Buoyant vortex rings. *Proc. Roy. Soc. A*, 239:61–75.

Turner, J. S. (1960). A comparison between buoyant vortex rings and vortex pairs. *J. Fluid Mech.*, 7:419–432.

Turner, J. S. (1964). The flow into an expanding spherical vortex. *J. Fluid Mech.*, 18:195–208.

Turner, J. S. (1973). *Buoyancy effects in fluids*. Cambridge University Press.

Turner, J. S. (1986). Turbulent entrainment: the development of the entrainment assumption, and its application to geophysical flows. *J. Fluid Mech.*, 173:431–471.

Vladimirov, V. A. and Tarasov, V. F. (1979). Structure of turbulence near the core of a vortex ring. *Sov. Phys. Dokl.*, 24:254–256.

Walters, J. K. and Davidson, J. F. (1962). The initial motion of a gas bubble formed in an inviscid liquid. Part 1. The two-dimensional bubble. *J. Fluid Mech.*, 12:408–416.

Walters, J. K. and Davidson, J. F. (1963). The initial motion of a gas bubble formed in an inviscid liquid. Part 2. The three-dimensional bubble and the toroidal bubble. *J. Fluid Mech.*, 17:321–336.

Weigand, A. and Gharib, M. (1994). On the decay of a turbulent vortex ring. *Phys. Fluids*, 6:3806–3808.

Widnall, S. E. and Bliss, D. B. (1971). Slender-body analysis of the motion and stability of a vortex filament containing an axial flow. *J. Fluid Mech.*, 50:335–353.

Widnall, S. E., Bliss, D. B., and Tsai, C.-Y. (1974). The instability of short waves on a vortex ring. *J. Fluid Mech.*, 66:35–47.

Widnall, S. E. and Sullivan, J. P. (1973). On the stability of vortex rings. *Proc. Roy. Soc. A*, 332:335–353.

Widnall, S. E. and Tsai, C.-Y. (1977). The instability of the thin vortex ring of constant vorticity. *Phil. Trans. R. Soc. Lond. A*, 287:273–305.

Won, S. and Lee, C. (2020). Simulation of the mushroom cloud generated from a high-energy explosion using large-eddy simulation. *J. Mech. Sci. Tech.*, 34:2443–2453.

Woodward, B. (1959). The motion in and around isolated thermals. *Quart. J. R. Met. Soc.*, 85:144–151.

Yih, C.-S. (1965). *Dynamics of Nonhomogeneous Fluids*. The Macmillan Company.

Zeldovich, Y. B. and Raizer, Y. P. (2002). *Physics of shock waves and high-temperature hydrodynamic phenomena*. Dover Publications.

Zhao, B., Law, A. W. K., Lai, A. C. H., and Adams, E. E. (2013). On the internal vorticity and density structures of miscible thermals. *J. Fluid Mech.*, 722:R5.